

Bottom-up

Self-assembly and Growth of Nanostructures, Molecular Architectures and Taylored Molecules

| | |
|--|----|
| Transport Processes at Nano-Patterned Surfaces – an Atomic View | 13 |
| Surfactant-Mediated Epitaxy | 20 |
| New Developments of the MOVPE Process Technology | 28 |
| The Importance of Many-Body Effects in the Clustering of Charged Zn Dopant Atoms in GaAs | 33 |
| Quantitative High-Resolution Transmission Electron Microscopy of LT-grown AlAs/GaAs:Be Heterostructures ... | 38 |
| “Live” Observations of the Growth of Nanostructures | 43 |
| Nanowires and Nanorings at the Atomic Level | 49 |
| 2D Supramolecular Electrochemistry and Nanostructures ... | 53 |
| Fullerenes: Taylored Molecules for New Materials | 60 |





Transport Processes at Nano-Patterned Surfaces – an Atomic View

With evermore shrinking sizes of microelectronic devices experimental and theoretical studies on mechanisms of self-assembly and on the stability of nano-patterns have gained importance. A crucial aspect of these topics is the atomic transport at surfaces and interfaces. Control and utilisation of these processes in nano-patterning require the understanding of all aspects on the atomic level: Hopping of individual atoms on surfaces, concerted motion of several atoms, movement of entire two- or three-dimensional clusters, mass transport across atomic steps, energies of various defects as driving forces for coarsening processes, relations between fluctuative and dissipative motion, the effect of electrical currents on atomic transports, the effect of the chemical environment. Discovery and analysis of the crucial steps is significantly impeded by the fact that in most cases these decisive steps are a vanishingly small minority. This is illustrated with the help of a few characteristic estimates for the order of magnitude in a typical coarsening process. The numbers are calculated for the coarsening process after deposition of a few monolayers of Cu on a Cu(111) single crystal surface, but they are characteristic for other materials as well.

TASK





Number of individual atom hopping processes during coarsening:

- 10^{16} single atom hops alongside steps
- 10^{16} detachments of atoms from kink sites to become adatoms at the step edges
 - Diffusion along steps is fast
- 10^{10} single atom hops on terraces
- 10^8 detachments of atoms from kink sites to become adatoms on terraces
 - Ostwald ripening within a single terrace is moderately fast
- 10^5 single atom hops over step edge
 - The interlayer mass transport is the slowest of all
Only this last process effectuates the layer-by-layer film growth

To find and to analyze this minute minority of crucial events seems to be a "mission impossible" – but in this laboratory we succeeded by recently developed advanced experimental and theoretical techniques.

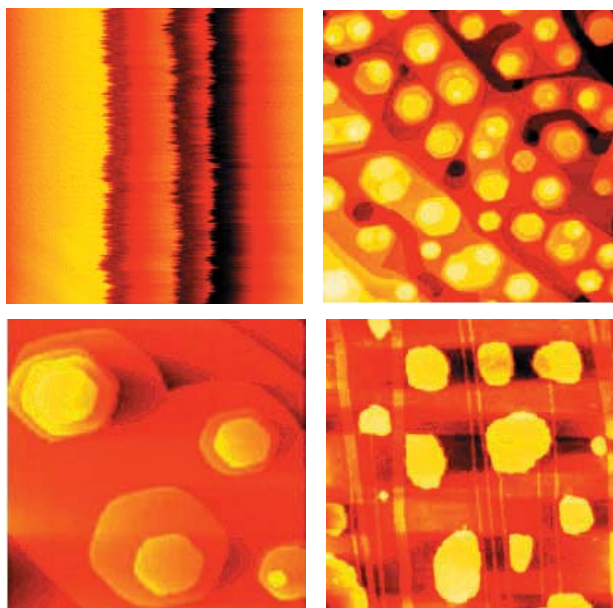
APPROACH

Growth and decay of nano-patterned surfaces in ultrahigh vacuum and at the solid liquid interface are studied using advanced STM-technologies which enable to record "in vivo" movies composed of up to 1000 images at variable temperatures. The real time span can range from a few minutes to 24 hours, remaining on the same spot of the sample. These movies are analysed with the help of special image analysis routines which extract spatio-temporal positions of steps and islands. The results are condensed into mathematical frameworks, allowing the application of advanced methods of statistical physics. The structural changes between the experimental observations form movies, which are determined by the underlying atomic processes. Without direct observation of the individual processes, intrinsic energetic para-

meters can be extracted from the experiments. Special emphasis is placed on the comparison of observations with theoretical models for surfaces in ultrahigh vacuum (UHV), but also to observations in a liquid electrolyte ambient. Here, the goal is to come to a better understanding of the influence of the liquid environment, of the electrolyte chemistry and of the electrode potential on atomic transport.

Our results are best illustrated by a sequence of STM-movies for which the reader is referred to <http://www.fz-juelich.de/isg/isg3/Giesen/ag-giesen1.htm#Atomic>.

So far we have focussed on homoepitaxial systems of copper, silver and gold in UHV, and also studies of the same materials in H_2SO_4 - and HClO_4 -electrolytes. Several novel features of transport processes were discovered, for example mass transport via vacancy hopping or interlayer mass transport via "atomic land-slides". Future systems will include transition metals and heteroepitaxial systems. In the following we give a short summary of key results. The images shown are available on our web site. We suggest to bring them to life by visiting the web site.



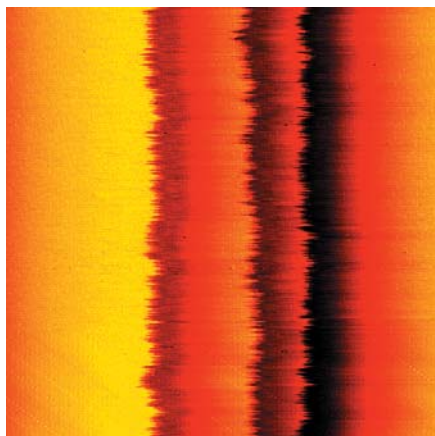
RESULTS

APPETISERS

See the animated process:
<http://www.fz-juelich.de/isg/isg3/Giesen/ag-giesen1.htm#Atomic>

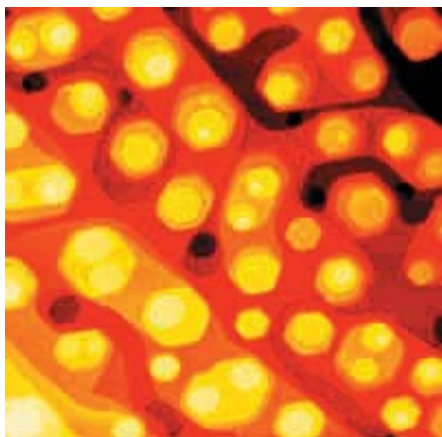


Video-Images



The video shows a sequence of 155 individual scanning tunneling microscopy (STM) images total. Each image took about 30s for recording. Hence, the video covers a real time of about 90 minutes. You see three double layer high, parallel steps on a Cu(111) surface at 27°C. The displayed surface area is 24x24 nm² and the surface height decreases from left to right. Due to atomic motion at the step edges, the steps do not remain straight and immobile, but undergo thermal fluctuations around their equilibrium position. From the statistical analysis of the time dependence of such equilibrium fluctuations one may deduce information about the individual atomic hopping processes occurring at the step edges.

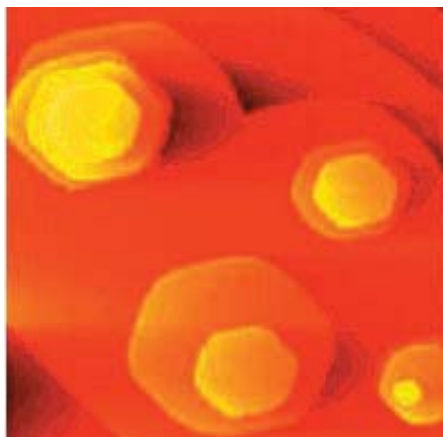




Video 2
Island coarsening

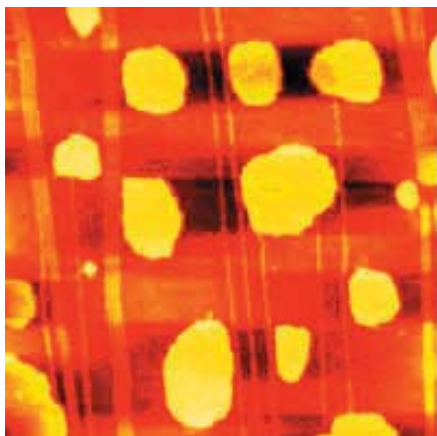
The movie shows a $150 \times 150 \text{ nm}^2$ area of a Cu(111) surface at 41°C after deposition of about 20 monolayers of copper. Due to the crystallographic symmetry of the (111) surface, almost hexagonal islands of multiple atomic layer height are formed. The islands are separated by holes, so-called vacancy islands, and several layer deep grooves. Driven by the higher chemical potential of atoms at step edges, in particular curved steps the surface undergoes a coarsening process. Holes and grooves are filled by atoms transported from the top layers of islands into the deeper layers. Note also the fast Brownian-like motion of entire islands! From the statistical analysis of the time dependence of such ripening and coarsening phenomena one may deduce information about the motion of single atoms on the surface. The movie shows the surface evolution during coarsening over a time span of approximately 13 hours. Such a movie includes about 1500 individual scanning tunnelling microscopy (STM) images. In order to record precisely the same surface area over such a long time span, a high-quality STM with high thermal drift stability is required!





Video 3
Atomic landslide

The movie shows a $200 \times 200 \text{ nm}^2$ area of a Cu(111) surface at 36°C after deposition of several monolayers of copper. The deposited copper forms monolayer-layer high hexagonal islands. These islands are mobile due to atomic diffusion along the island edges and due to attachment/detachment of atoms. The latter process causes also the so-called "Ostwald-ripening" of islands which leads to a growth of large islands and to the shrinking of small islands. This process is normally hindered for small islands on top of large islands. The reason for this is the existence of a step edge barrier for atomic diffusion across island edges on (111) surfaces. This movie, however, shows that sometimes this step edge barrier may be bypassed and the shrinking of small top layer islands is accelerated by a factor of 100. We called this event an "atomic landslide". In the movie, the white arrow indicates an island on top of another island which hardly shrinks in size for hours. After about eight hours, the top island approaches the perimeter of the lower island and then eventually the top island vanishes within very short time.



Video 4
Au(100) Reconstruction

The movie shows a sequence of electrochemical scanning tunnelling microscopy (EC-STM) images of a Au(100) surface in 50 mM H_2SO_4 with monatomic high Au islands at room temperature. The surface area is $110 \times 110 \text{ nm}^2$. At low electrode potentials, the Au(100) exhibits a quasi-hexagonal reconstruction with a higher atomic density in the surface layer than the normal (1x1) structure of the (100) surface. Increasing the electrode potential to more positive values, the reconstruction is lifted and monatomic high islands are formed. These islands are not static but reveal a high mobility. This mobility is due to hopping of atoms along the island perimeter which causes also visible fluctuations of the island perimeter around an average island shape. For this movie, the electrode potential has first been increased to +350 mV vs. the SCE (Saturated Calomel Electrode) reference to create islands on the Au(100) surface. Then, the potential has been stepped back again to -200 mV where the surface reconstruction is re-established. The islands decay due to the formation of the denser reconstructed layer. Reconstruction lines (which appear bright in the movie) are formed and the islands are "eaten up". From these movies it is possible to analyse the kinetics of the formation of the reconstruction lines and the atomic hopping processes involved.

Margret Giesen, Harald Ibach

AUTHORS



Surfactant-Mediated Epitaxy

INTRODUCTION

Electronic and optoelectronic devices need specific materials and heterostructures. Unfortunately, materials with vastly different physical properties (structure, lattice constants) do not naturally grow epitaxially layer by layer, as needed for lasers, light emitting diodes or high speed transistors. An important example is the growth of Ge on Si. The lattice misfit of $\approx 4\%$ triggers the growth of large three-dimensional Ge islands, which render the Si-Ge system useless for applications. Experimentalists have found a cure: Depositing a (sub-)monolayer (ML) of group-V metal atoms (As, Sb, Bi) prior to the Ge deposition drastically changes the Ge surface states, the diffusion and the growth characteristics. Such layers are called surfactant ("surface active agent")-layers. With their help atomically flat Ge films can be grown on Si(111). In 1999 a MOSFET with an active p-doped Ge layer on a Si(111) substrate has been produced successfully.

APPROACH

Microscopic Picture

The "surfactant effect" is not yet fully understood on the molecular level. (i) Surfactant layers change the surface structure of the semiconductor. For instance, 1 ML of As changes the famous (7x7) reconstruction of the clean Si(111) surface to a nearly undistorted (1x1) structure of a bulk terminated Si crystal. With different surfactants short periodic structures are found on the low-index surfaces of the elemental semiconductors: e.g. Si(111):Sb, Bi ($\sqrt{3}\times\sqrt{3}$), Ge(111):Sb (2x1). (ii) The surface energy is lowered due to the additional electrons of the surfactant atoms: The energetically unfavorable Si, Ge dangling bonds on the clean surfaces are replaced by filled lone pair orbitals at the covered surfaces. As an important consequence the surfactant atoms remain at the surface during film growth, they "float on top". (iii) The kinetics of the deposited atoms is changed. Due to surfactant "passivation" the activation barrier for surface diffu-

sion is expected to decrease compared to clean surfaces. But, since the surfactants float on top of the growing crystal, every deposited atom eventually has to be incorporated to a substitutional site under the surfactant layer by exchange with a surfactant atom. The microscopic kinetic parameters cannot be extracted directly from experiments. We shortly describe our theoretical activities aiming at a better understanding of the microscopic surfactant effects. Our calculations are based on density functional theory in the local density approximation,

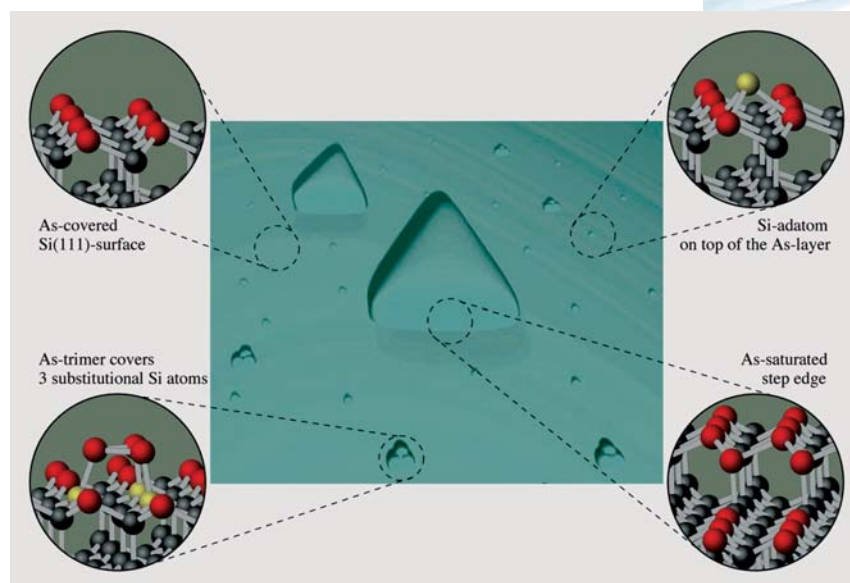


Fig. 1

Schematic view of a surfactant covered surface during growth. On the growing surface one finds single adatoms, agglomerates of different sizes and islands, terminated by steps. The blown-up figures show calculated structures on the As-covered Si(111) surface (As red, Si grey, additional Si atoms yellow) (i) The As-covered surface is terminated by a perfect double layer (DL). (ii) The equilibrium position of a single Si adatom is in the middle of the hexagonal ring above the As surface layer. By thermal activation adatoms can either migrate across the surface or are incorporated to a substitutional site in the As layer by exchange with an As atom. (iii) A cluster formed by three substitutional Si atoms (which locally completes the Si DL) is covered by a trimer of As atoms. (iv) Islands on the As-covered Si(111)-surface are terminated by steps which have the height of a DL. At the step edge all exposed Si atoms are replaced by As atoms.



representing the present state of the art in electronic structure calculations. We apply the planewave code EStCoMPP which was developed in Jülich. Figure 1 summarizes the structural information of the initial stages of growth on a surfactant covered surface.

RESULTS Diffusion and Exchange Compete

The kinetics of adatoms is characterized by a competition between on-top diffusion, the incorporation process, and possibly the reexchange to an adatom position. We have determined the paths and activation energies for diffusion of Si and Ge atoms on top of the As layer on As-passivated Si(111), and for exchange with an As atom[1]. Figure 2 shows the energy variation along the diffusion and exchange paths, respectively. From the

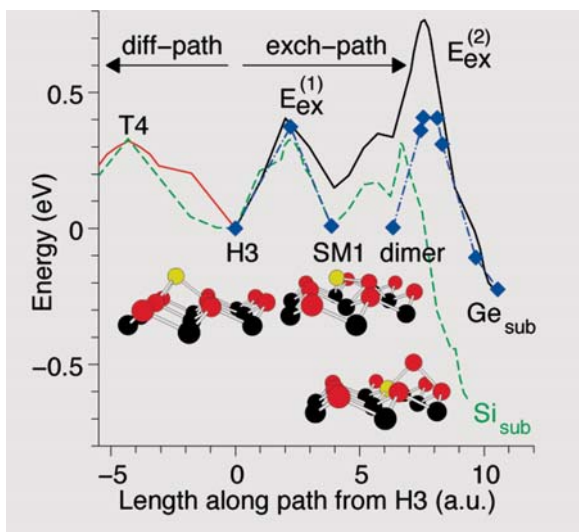


Fig. 2
Variation of energy along the diffusion path (to the left of H3) and along the exchange path to the substitutional configuration (to the right). Compared are the energies for Si (dashed line) and Ge (full line) on a Si(111):As substrate and for Ge on a Ge(111):As substrate (diamonds)). The atomic configurations for important minima are shown as insets: H3: adatom equilibrium; T4: diffusion saddle point; E_{ex}⁽¹⁾: saddle points on exchange path; Ge-As-dimer; Si(Ge)_{sub}: substitutional Si(Ge) and As adatom (yellow: Si(Ge) adatom; red: As; black: Si bulk).

relation of the energy barriers we can conclude that homoepitaxy and heteroepitaxy on Si(111):As proceed by different mechanisms. (i) Si adatoms are readily incorporated under the As-layer because the activation energies for diffusion and exchange are nearly equal. The long range migration of Si adatoms is governed by the reexchange process from the equilibrium substitutional position under the As layer. This barrier is higher than for diffusion on the clean Si(111) surface. This explains the much higher island density experimentally found for homoepitaxy on As (and Sb) covered Si(111) than on the clean Si(111) surface. Homoepitaxy on Si(111):As proceeds only via nucleation and growth of two-dimensional Si islands on the terraces. (ii) On the other hand, for Ge adatoms on Si(111):As the barrier for exchange is much higher than for diffusion. Ge adatoms thus can diffuse far on top of the As layer and can even reach existing steps before being incorporated. Growth can proceed by a mixture of step flow and island nucleation on the terrace, depending on the efficiency of As passivation of steps. We have also shown that the exchange probability of a Ge adatom increases when the Ge film grows and relaxes, and for a fully relaxed As-covered Ge film we find a similar situation as for homoepitaxy of Si.

Clusters and Islands

Scanning tunneling microscopy (STM) and extensive *ab initio* calculations of Si_n -clusters ($n \leq 12$) reveal a different behavior of the two surfactants As and Sb[2]: On As-covered Si(111), one exclusively finds twodimensional islands with double-layer height which show the (1x1) terrace structure. On Sb-covered Si(111) the islands show two different reconstruction patterns: at the rim of the islands a (1x1)-structure appears, while in the center the $(\sqrt{3} \times \sqrt{3})$ terrace structure is observed. The different growth behavior for homoepitaxy on As- and Sb-covered Si(111) found in experiments can be understood on the basis of the calculated formation energies for Si_n -clusters, as shown in Fig. 3, and Fig. 4. (i) On Si(111):As(1x1) the observed double layer growth starts already at a cluster size of four Si atoms. (ii) On Si(111):Sb(1x1) individual Sb trimers grow on top of a locally



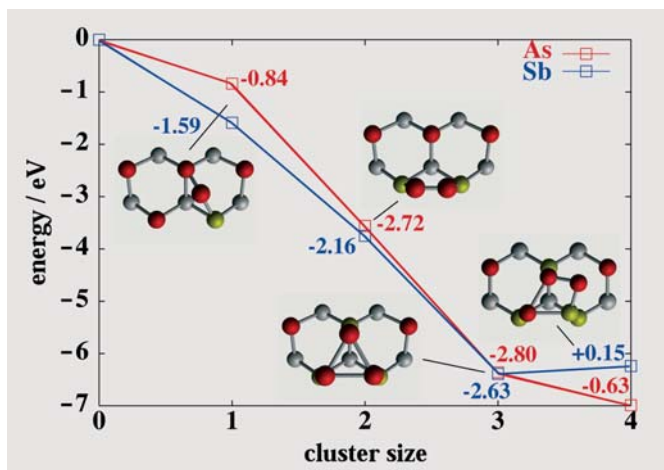


Fig. 3: Development of small Si_n -clusters during homoepitaxy. On (As, Sb)-covered $\text{Si}(111)(1 \times 1)$ for $n=1-4$ (top-views of the clusters are shown as inserts; Si atom in cluster: yellow, Si bulk: grey, As, Sb: red). Plotted are the calculated energies which are gained by forming a Si_n -cluster from n single Si adatoms in the H3 position on top of the surfactant layer. The listed energies (in eV) are the differences $\Delta E^{(n)}$ gained by forming a Si_n -cluster from a Si_{n-1} -cluster plus a single incorporated Si atom. $\text{Si}(111):\text{As}$ (red lines): The energies monotonically decrease up to $n=3$, the 4th Si atom is attached to the As trimer. $\text{Si}(111):\text{Sb}$ (blue lines): The energies decrease up to $n=3$, but $\Delta E^{(4)}$ is positive. The forth Si atom is not attached to the Sb trimer.

completed Si double-layer nucleating the more favorable $(\sqrt{3} \times \sqrt{3})$ structure by single layer growth. (iii) On the $\text{Si}(111):\text{Sb}(\sqrt{3} \times \sqrt{3})$ terrace structure double layer growth is inhibited geometrically and kinetically: (a) sufficiently large (1×1) cluster have to be established to support (new) Sb trimers; (b) there is a nucleation barrier for 2nd layer trimer growth. This explains the observed (1×1) rim at all Si islands on Sb-covered $\text{Si}(111)$, see Fig. 4.

STM Images of Terrace Steps

The step structure on surfactant-covered surfaces has an important influence on the competition between island nucleation on the terrace vs. step flow. Step structures can be measured by

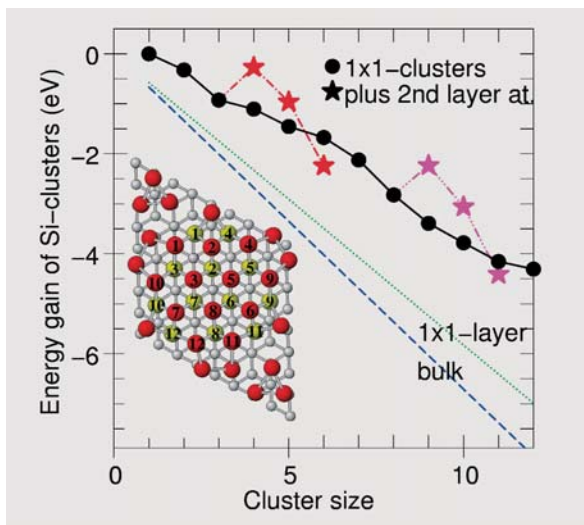
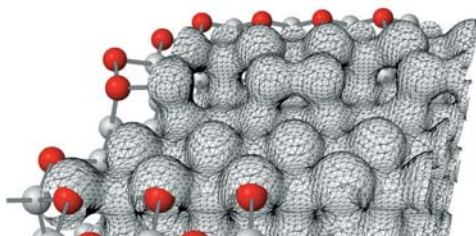
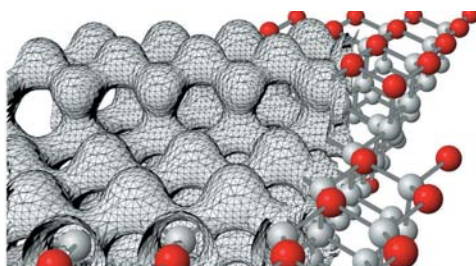
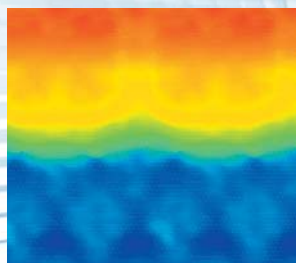
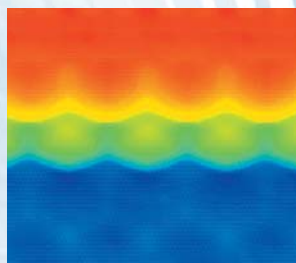


Fig. 4

On Sb-covered Si(111) ($\sqrt{3}\times\sqrt{3}$) for $n=1-12$ (Si-cluster: yellow, Si bulk: grey, Sb: red). Plotted are the calculated energies (full points) gained by forming an Sb-covered Si_n -cluster with (1x1) surface structure from n single incorporated Si atoms. The dot-dashed lines connect the calculated energies (full stars) when additional (up to 3) Si atoms are built into the second layer: red: on top of a Si_3 cluster; magenta: on top of a Si_8 cluster. The dotted lines are the energies obtained when each atom in a cluster would gain the energy per atom of a full (1x1) layer on the ($\sqrt{3}\times\sqrt{3}$) Si(111):Sb surface (green), and of the Si bulk (blue), respectively. The insert shows the top-view of the Si_{12} (1x1)-cluster (numbered atoms, yellow Si, red Sb). The numbers indicate the sequence of attachment.

atomically resolved STM images. For the extraction of atomic positions a theoretical simulation of the STM images is necessary. From our calculations [3] we find that the lowest energy structures for both experimentally observed step orientations ($(11\bar{2})$ and $(\bar{1}\bar{1}2)$) on Si(111):As are the As-passivated steps shown in Figure 5. The exposed second layer Si atoms at the step edges are replaced by As atoms. At the $(11\bar{2})$ step this leads to a stable configuration since the As atoms are in a naturally threefold coordinated position, i.e. the As atoms at the step edge are in equivalent positions as on the (111) oriented terraces. At the $(\bar{1}\bar{1}2)$ step the As atoms are only twofold coordinated in the unrelaxed positions. They form dimers to saturate their



bonds. The simulated constant-LDOS STM-images closely relate to the measured constant-current STM-images. Results are shown in Figure 5. – For negative bias voltage, when the occupied states of the surface contribute to the tunneling current, the lone-pair occupied states of the exposed As atoms make a major contribution and the two step orientations can clearly be distinguished. – For positive bias voltage, when the unoccupied states contribute, the differences are nearly completely washed out.

Fig. 5

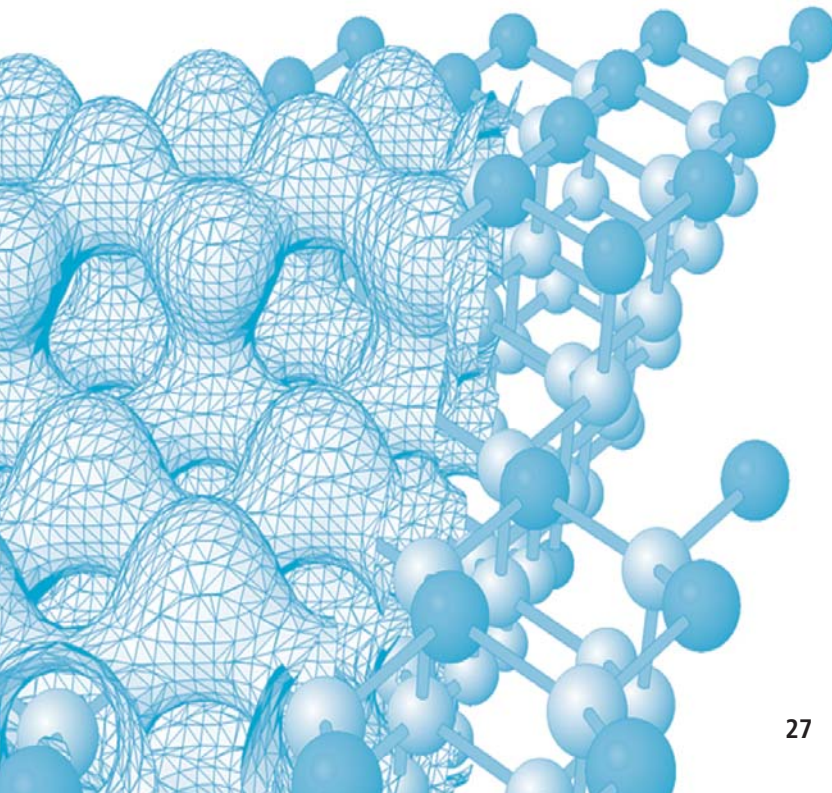
Structure of the As-passivated $(11\bar{2})$ step (upper panels) and $(\bar{1}\bar{1}2)$ step (lower panels) on Si(111):As. For both orientations (left) the simulated STM image for a bias voltage of -1.5 V (occupied states image), and (right) the atomic structure and the electron density contour which characterizes the bonding character at each atom, are shown. Si atoms are gray, As atoms red spheres. On the terraces the As atoms replace the Si atoms of the upper half of a double layer. At the terrace edge the exposed second layer Si atoms are replaced by As. In the STM-image the As atoms contribute with the vacuum lobe of the lone-pair electron wavefunctions. Note, that for the As atoms at the step edges the maxima in the tunneling current do not coincide with the surface projected positions. At the $(11\bar{2})$ step the exposed 2nd layer As atoms are clearly placed symmetrically in the middle between the As atoms in the upper layer. At the $(\bar{1}\bar{1}2)$ step the As dimers show up as broad maxima resembling the superstructure along this step edge.

- [1] K.Schroeder, A. Antons, R.Berger, S. Blügel:
"Surfactant mediated heteroepitaxy versus homoepitaxy:
Kinetics of group-IV atoms on As-passivated Si(111) and
Ge(111)", Phys. Rev. Lett. 88, 046101 (2002).
- [2] A. Antons, K.Schroeder, B. Voigtländer, V. Cherepanov,
R. Berger, S. Blügel:
"Element Specific Surface Reconstructions of Islands During
Surfactant-Mediated Growth on Si(111)",
Phys. Rev. Lett. 89, 236101 (2002).
- [3] A. Antons, R. Berger, B. Voigtländer, K.Schroeder, S. Blügel:
"Structure of Steps on As-covered Si(111): STM images and
ab initio calculations", in preparation.

Kurt Schroeder, Armin Antons, Bert Voigtländer

REFERENCES

AUTHORS

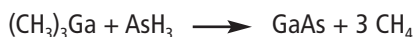




New Developments of the MOVPE Process Technology

INTRODUCTION

Metalorganic vapor phase epitaxy (MOVPE) is an important industrial process for the growth of nanostructures and the production of III/V compound semiconductors. In this growth process a carrier gas is used to transport the group III-trimethyl compounds and the group V hydrides to the heated zone of the reactor. Here they decompose in the gas phase as well as on the substrate surface to form the highly pure III/V alloys according to the following equation for GaAs:



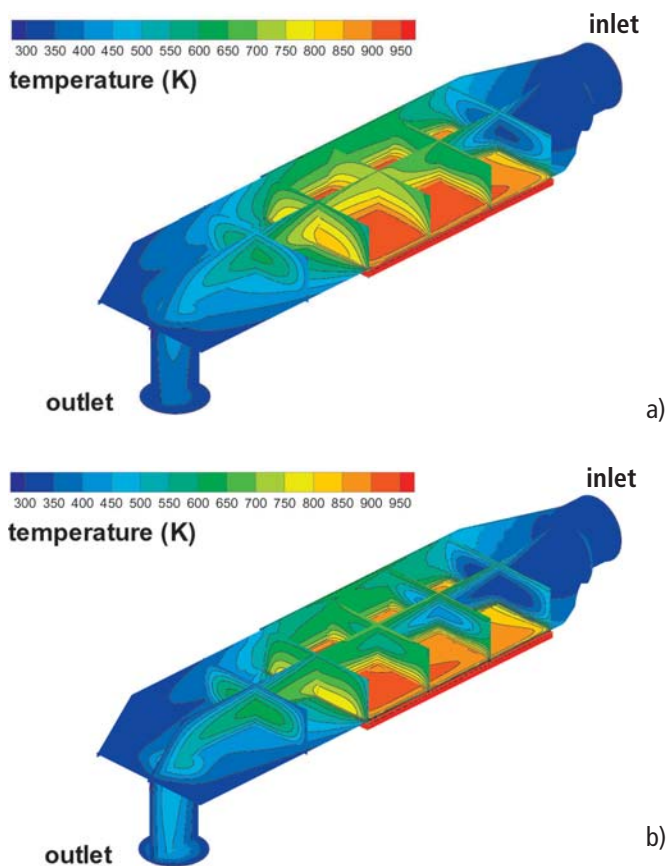
The influence of the carrier gas on growth was first recognized in Jülich. Conventionally hydrogen gas had been used. Since the carrier gas is the medium in which the gas phase reactions take place, its chemical characteristics, as reactivity towards reaction educts, by-products and products, and its physical properties, as thermal conductivity, heat capacity, viscosity and density, determine the growth and also to some extent the material purity. In our experiments the hydrogen carrier gas was replaced by nitrogen. A better growth process was achieved, leading to purer and more homogenous material. In addition, the overall laboratory safety was strongly increased.

APPROACH

However, a mere replacement of the hydrogen flow by nitrogen would not be successful, because these gases differ strongly in their properties. Therefore the detailed gas flow in the reactor had to be analyzed and optimized. In addition, a deeper understanding of the growth process was necessary. The influence of the carrier gas on the temperature distribution was studied as well as the influence on the local growth rate. This was achieved by performing experiments and numerical modeling.

Furthermore, the surface reconstruction was evaluated experimentally. These studies elucidated, why we achieved significant advantages using our new processing scheme.

Our experiments using nitrogen show, that the gas flow should be reduced to less than 50%, if compared to hydrogen. Only then a high quality layer growth is achieved. Modeling results of the temperature distribution in the reactor under flow conditions optimized for best material quality and homogeneity are shown in Figs. 1a and 1b for the horizontal reactor. In this picture, the temperature profile is color coded, ranging from red (hot) to blue (cold). Due to the lower thermal conductivity of nitrogen compared to hydrogen, a so-called "cold finger" is observed near the gas inlet: it takes a longer distance until the nitrogen gas phase reaches the same temperature as it would be for hydrogen.



RESULTS

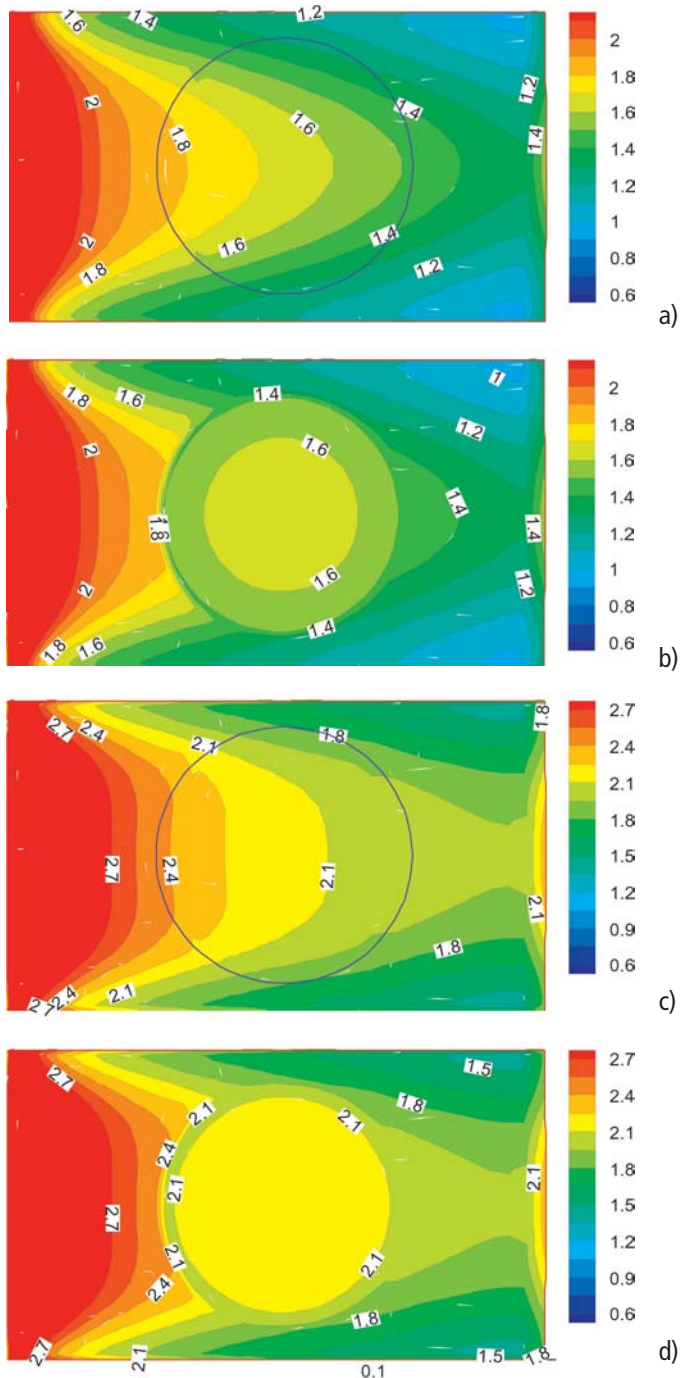
Fig. 1

Computed temperature distribution in the gas phase in a horizontal reactor at 700°C deposition temperature and at optimized gas flows for a) hydrogen and b) nitrogen carrier gas, respectively. For visualization, a grid was put over the susceptor and the reactor is presented partly open (the ceiling and one sidewall are missing). The temperature distribution towards the ceiling of the reactor is shown only along the imaginary grid lines. A cold finger is observed near the reactor inlet for nitrogen carrier gas.



Fig. 2

Computed growth rate distribution in $\mu\text{m/h}$ for AlGaAs growth in a horizontal reactor under optimal growth conditions for (a) and (c) without substrate rotation and (b) and (d) with substrate rotation for hydrogen and nitrogen carrier gas, respectively. The gas phase is fully developed for hydrogen carrier gas demonstrated by the parabolic growth rate profile on the location of the substrate. For nitrogen carrier gas an increase in uniformity is observed due to the more block-like flow profile for the undeveloped gas phase.



The experiments showed that the replacement of the carrier gas hydrogen for nitrogen leads to an enormous decrease of standard deviation of layer thickness from 5% to <1%. Figs. 2a and 2c show the growth rate distribution on the substrates resulting from three-dimensional computations without substrate rotation and 2b and 2d with substrate rotation under flow conditions optimized again with respect to material quality and homogeneity. The growth rates are translated into colors ranging from red for higher to blue for lower growth rates. The computation gives insight into the mechanism responsible for growth rate uniformity in horizontal tube reactors. The flow profile in the rectangular reactor tube develops during the so-called hydrodynamic entrance length from a block-like profile close to the reactor entrance into a parabolic profile confined by the side walls of the reactor. The length after which this happens is eight times longer for nitrogen than for hydrogen due to the eightfold higher convective to conductive heat transfer ratio. Under the optimized flow ratio, the gas phase is not fully developed for nitrogen carrier in contrast to hydrogen. The great increase in uniformity for nitrogen carrier gas compared to hydrogen is therefore due to the undeveloped gas phase.

Why does the purity of the layers increase, if nitrogen is used as the carrier gas ?

The answer was found by performing in situ reflective anisotropy spectroscopy during the growth process. This characterization technique is sensitive to surface reconstructions which correlate with the stoichiometry of the surface. The concentration of group V elements increases in nitrogen as compared to hydrogen - an indication that decomposition of the hydrides is enhanced in nitrogen carrier gas. This also means that the by-product atomic hydrogen also increases in the nitrogen atmosphere. It is responsible for the higher purity of the layers deposited in a nitrogen atmosphere. Since its first demonstration in Jülich, the nitrogen carrier gas has been used by a number of groups for various III/V-materials. One of the latest materials are the group III nitrides for light emitting diodes and laser applications. It is not pos-





sible to grow these compound semiconductors without the use of an inert carrier gas such as nitrogen, since for optical devices only this process allows the incorporation of the indispensable element indium into GaInN.

REFERENCES

“MOVPE gets green signal”

H. Hardtdegen, P. Giannoules

III-Vs Review 11 No. 5 (1998) 34.

“Modeling and experimental verification of deposition behavior during AlGaAs growth: a comparison for the carrier gases N_2 and H_2 ”

M. Dauelsberg, H. Hardtdegen, L. Kadinski, A. Kaluza and P. Kaufmann

J. Cryst. Growth 223 (2001) 23.

“In situ characterization of GaAs growth in nitrogen atmosphere during MOVPE: a comparison to hydrogen atmosphere”

H. Hardtdegen, M. Pristovsek, H. Menhal, J.-T. Zettler, W. Richter, D. Schmitz

J. Cryst. Growth 195 (1998) 211.

AUTHOR

Hilde Hardtdegen

The Importance of Many-Body Effects in the Clustering of Charged Zn Dopant Atoms in GaAs

The ability to incorporate dopant atoms with precisely controlled concentrations and spatial distributions is essential for various technological applications of semiconductor materials. The efforts towards device miniaturization continue, but the approaches are becoming increasingly difficult. In fact, dopant incorporation in submicrometer- and nanometer-scale systems is ultimately governed by the intrinsic interactions between the dopant atoms. The generally accepted view is that the charge of a dopant atom is screened by the charge carriers in the host semiconductor, resulting in a repulsive screened Coulomb interaction between the dopants. Such a repulsion in turn will lead to a rather homogeneous distribution of the dopant atoms in the semiconductor. The technologically and scientifically intriguing question is, however, if dopant atoms are really homogeneously distributed on the nanometer scale.

Our experimental approach is based on the so called cross-sectional scanning tunneling microscopy (XSTM) technique. This method is based on the cleavage of crystals in ultrahigh vacuum, which allows to expose a clean surface providing a cross-sectional view through the material. The dopant atoms (and defects) inside of the material are then observable by STM on the cleavage surface with atomic resolution. This technique allows to identify the positions of dopant atoms with atomic precision in three dimensions, i.e., also in layers deep below the surface, due to the presence of a long range screened Coulomb potential around each dopant atom. For an overview see ref. 1.

INTRODUCTION

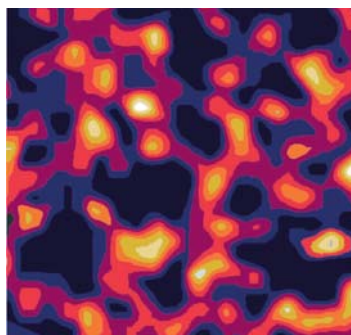
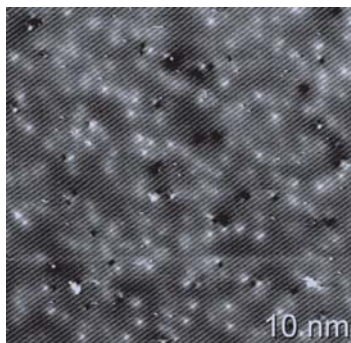
APPROACH





Fig. 1

(a) Scanning tunneling microscope image of a (110) cleavage surface of Zn-doped GaAs acquired at 2.4 V. A long range contrast variation is superposed onto the atomic-scale corrugation of the atomic rows along the [100] direction. The bright and dark contrast features are dopant atoms and vacancies, respectively. (b) positions of the dopant atoms in (a). (c) Local concentration of the dopant atoms. A high concentration is shown as yellow contrast, whereas the local concentration of dopants is a factor of 8 lower in the dark areas. The images show a clustering of the dopant atoms.



For the present task we investigated several Zn-doped GaAs crystals with different carrier concentrations (n) ranging between 2.5×10^{18} and $2.5 \times 10^{20} \text{ cm}^{-3}$. The Zn dopant atoms were introduced into the crystals during growth ($n < 10^{20} \text{ cm}^{-3}$) or by Zn diffusion at $\approx 1180 \text{ K}$ ($n > 10^{20} \text{ cm}^{-3}$). After growth, the crystals were slowly cooled down to room temperature - with the exception of Zn diffused crystals, which were quenched to room temperature. Thus the dopant atoms reached an equilibrium at a freeze-in temperature of GaAs or in case of Zn-diffused material at $\approx 1180 \text{ K}$. Samples cut from the different crystals were cleaved in ultrahigh vacuum ($5 \times 10^{-9} \text{ Pa}$) and the isolated dopant atoms exposed on the (110) cleavage surfaces were imaged with atomic resolution by XSTM (Fig. 1a). Localized bright contrast features arise from isolated dopant atoms, whose charge gives rise to a local charge redistribution and potential variation imaged by the scanning tunneling microscope. After identification of the positions of the dopant atoms (Fig. 1b) we calculated the local dopant concentration (Fig. 1c) and the pair-correlation function $c(r)$ (Fig. 2). The negative logarithm of the pair correlation func-

tion by XSTM (Fig. 1a). Localized bright contrast features arise from isolated dopant atoms, whose charge gives rise to a local charge redistribution and potential variation imaged by the scanning tunneling microscope. After identification of the positions of the dopant atoms (Fig. 1b) we calculated the local dopant concentration (Fig. 1c) and the pair-correlation function $c(r)$ (Fig. 2). The negative logarithm of the pair correlation func-

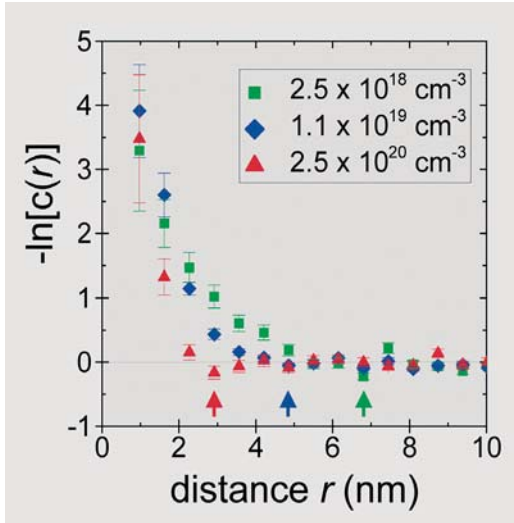


Fig. 2
Negative logarithm of the pair correlation function (equivalent to the mean force potential divided by kT) for three carrier concentrations.

tion is proportional to the so called mean force potential. In case of low dopant concentration (i.e., the average distance between dopants must be much larger than the extent of the interaction potential), the mean force potential equals the pair interaction potential. Since this approximation is not valid in our case (see results below), we used Monte Carlo simulations to extract the pair interaction potential, in particular the screening length of the screened Coulomb potential (Fig. 3).

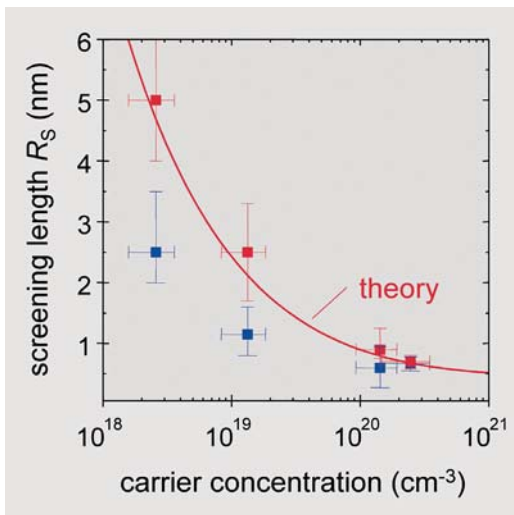


Fig. 3
Values for the screening lengths R_s determined from the data in Fig. 2 as a function of the carrier concentration (blue squares). The solid line represents the theoretical screening length. The red squares show the screening length corrected for many-body interactions.



RESULTS

The cross-sectional scanning tunneling microscopy images such as that shown in Fig. 1, directly demonstrate that negatively charged Zn dopant atoms in GaAs are inhomogeneously distributed and form clusters of dopant atoms with dimensions of about 10 nm. This is the first direct observation of clustering of dopant atoms on such a length scale [2]. At the first sight, the clustering behavior seems to suggest the existence of a possible attractive interaction in addition to the screened Coulomb repulsion between the dopants. But our quantitative analysis of the dopant distributions by Monte Carlo simulations showed that the effective attraction actually results from strong many-body effects in the repulsive dopant-dopant interactions. The many body effects lead to a small minimum of the negative logarithm of the pair correlation function or the mean force potential marked by arrows in Fig. 2. The minimum is in addition to the repulsive interaction, whose extension increases from 2 to 5 nm if the carrier concentration decreases from 2.5×10^{20} to $2.5 \times 10^{18} \text{ cm}^{-3}$. This reflects the repulsive screened Coulomb interaction between two equal charges and the carrier concentration dependence of the screening. It is well known that the charge of a dopant atom in a semiconductor is screened by the charge carriers, leading to a screened Coulomb potential surrounding each dopant:

$$V(r) = e / (4\pi\epsilon_0\epsilon_r) \cdot 1/r \exp(-r/R_s)$$

with R_s being the screening length, which is a function of the temperature and carrier concentration.

The effective screening length (i.e., that of the mean force potential) has been extracted from the experimental data of Fig. 2 and is shown as a function of the carrier concentration in Fig. 3 (blue squares). As expected, the screening length increases with decreasing carrier concentration. However, the data do not agree quantitatively with the theoretical values for the screening length (red solid line in Fig. 3) determined for a freeze-in temperature of 900 K. If we now take into account many-body effects in the otherwise repulsive interaction between the dopants, we can extract the real screening length of the

screened Coulomb potential surrounding an isolated dopant atom (red squares in Fig. 3), which agree well with the theoretical expectation. The good agreement of the screening length with estimates based on many-body effects and that from the classical screening theory indicates that the present system can be well described by the classical screening. The importance of many-body effects is found in an attractive part beyond a short-range repulsive core, which leads to the clustering of dopant atoms observed experimentally. This conclusion is consistent with the observation that clustering of dopant atoms occurs independent of the semiconductor material, growth conditions, dopant element, and the technique of dopant incorporation. Our study reveals a basic physical origin limiting the homogeneity of dopant atoms achievable in semiconductors. These clustering effects of dopant atoms are of great importance in nanostructures for electronic devices [3, 4].

- [1] Ph. Ebert, Surf. Sci. Reports **33**, 121 (1999).
- [2] Ph. Ebert, T. Zhang, F. Kluge, M. Simon, Z. Zhang, and K. Urban, Phys. Rev. Lett. **83**, 757 (1999).
- [3] N.D. Jäger, K. Urban, E. R. Weber, and Ph. Ebert, Phys. Rev. B **65**, 235202 (2002).
- [4] N.D. Jäger, K. Urban, E. R. Weber, and Ph. Ebert, Appl. Phys. Lett. **82**, in press (2003)

Philipp Ebert¹, Tianjiao Zhang^{2,3}, Fanying Kluge¹, Zhenyu Zhang^{2,3}, and Knut Urban¹

¹ Institut für Festkörperforschung,
Forschungszentrum Jülich GmbH, 52425 Jülich, Germany

² Department of Physics, University of Tennessee,
Knoxville, TN 37996

³ Solid State Division, Oak Ridge National Laboratory,
Oak Ridge, TN 37831-6032

REFERENCES

AUTHORS





Quantitative High-Resolution Transmission Electron Microscopy of LT-grown AlAs/GaAs:Be Heterostructures

INTRODUCTION

AlAs/GaAs multiple quantum wells (MQWs) epitaxially grown at rather low temperatures (LT) of about 200°C are of high research interest, because they show great promise for the fabrication of ultrafast electronic device structures. For the technology of these nanoscale systems it is essential to control the interface quality between as-grown layers on an atomic scale. Beyond this optimization of the epitaxial growth process, the interpretation of the electronic device characteristics necessitates a detailed understanding on the origin of structural modifications due to the thermal treatment during processing. The inherently high concentration of gallium vacancy point defects is regarded as the main limitation of LT-grown MQWs, since these vacancies also mediate the exchange of aluminium and gallium atoms across internal interfaces and, thus enhance the intermixing, if compared to layer systems grown at about 600°C, which is a standard deposition temperature. It is of special importance to develop new processing pathways to further improve the structural stability of LT-grown MQWs against the compositional mixing.

APPROACH

We investigate LT-grown AlAs/GaAs:Be MQWs doped with different beryllium concentrations in order to quantify the stabilization of their layer structure upon thermal treatment. As the nominal thicknesses of the AlAs layers are limited to a few nanometres, the morphology as expressed by the interface roughness between layers of different local aluminium concentration x_{Al} , quantitative high-resolution transmission electron microscopy (HRTEM) is the method of choice when measuring this param-

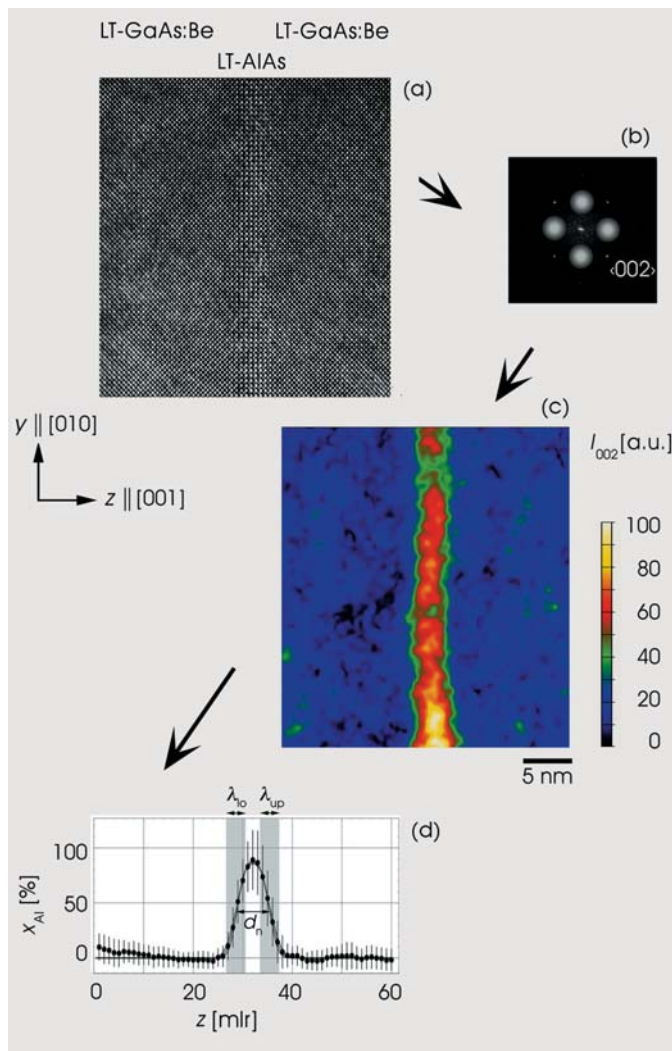


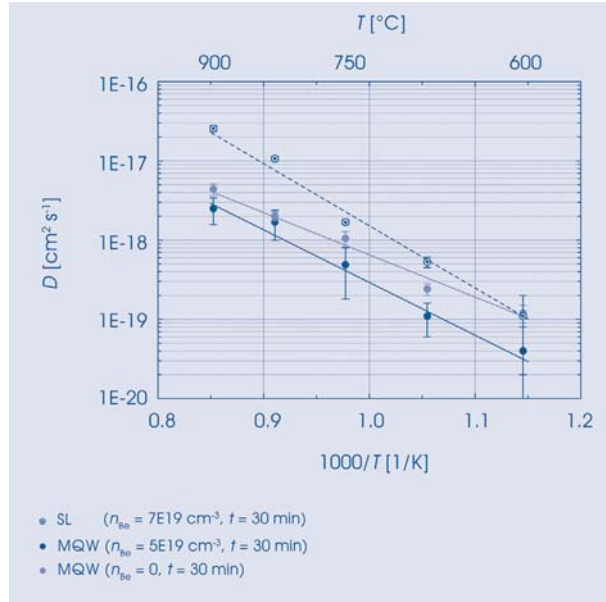
Fig. 1

(a) High-resolution micrograph taken under chemically sensitive imaging conditions showing an AlAs layer embedded in GaAs:Be annealed for 30 min at 750°C. (b) Diffractogram with the grey shaded areas indicating the positions of Gaussian apertures successively convoluted with the Fourier transform of the image and used to evaluate the (c) beam intensity distribution $I_{002}(x, z)$. (d) Compositional profile $x_{Al}(z)$ along the [001] growth direction. The solid curve represents a least square fit of the diffusion profile to the experimental data yielding $d_n = 6.73 \pm 0.30$ ML (monolayers), $\lambda_{10} = 2.09 \pm 0.29$ ML and $\lambda_{up} = 2.17 \pm 0.30$ ML for the nominal layer thickness as well as the interface roughness parameters at the lower and the upper interfaces, respectively.

ter in-line with the direct imaging of the atomic layer structure. For these purposes we record high-resolution micrographs under chemically sensitive imaging conditions and quantitatively analyse these images by specially developed image processing algorithms. As sketched in Fig. 1, this numerical technique basically implies measuring the (002) beam intensity distribution $I_{002}(x, z)$ from the high-resolution micrographs by reciprocal space extraction operations. Under optimized experimental imaging conditions this distribution carries direct information on the local aluminium content x_{Al} of the layers.



Fig. 2
Diffusion coefficient D (T)
measured for the intermixing
of aluminium and gallium;
solid curves represent
regression fits to the experi-
mental data obtained for
multiple quantum well
(MQW) and superlattice (SL)
systems doped with different
beryllium concentrations n_{Be} .



RESULTS

Microscopically measured data on the nominal thickness d_n of AlAs layers embedded in GaAs together with interfacial roughness parameters λ_{lo} and λ_{up} , cf. Fig. 1, of as-grown MQWs and of samples annealed at technologically relevant process temperatures are used as input parameters for the numerical evaluation of the diffusion coefficient $D(T)$ in dependence on the anneal temperature T applied. When using non-linear diffusion theory, our results clearly demonstrate a significantly reduced intermixing for highly doped LT-GaAs:Be compared to undoped LT-GaAs layers grown under identical conditions. Fig. 2 demonstrates that the activation enthalpies H for the intermixing process increases from 1.0 eV (LT-GaAs) to 1.4 eV (LT-GaAs:Be) when focusing on beryllium dopant concentrations $n_{\text{Be}} > 10^{19} \text{ cm}^{-3}$ while even higher values of 1.7 eV are found in case of ultrathin AlAs/GaAs:Be superlattices grown under similar conditions. Independent of the doping concentration, these values are extraordinary low compared to $H \approx 6 \text{ eV}$ as measured for AlAs/GaAs layer systems grown at standard temperatures and, hence, characterized by a rather small equilibrium concentration of gallium vacancies.

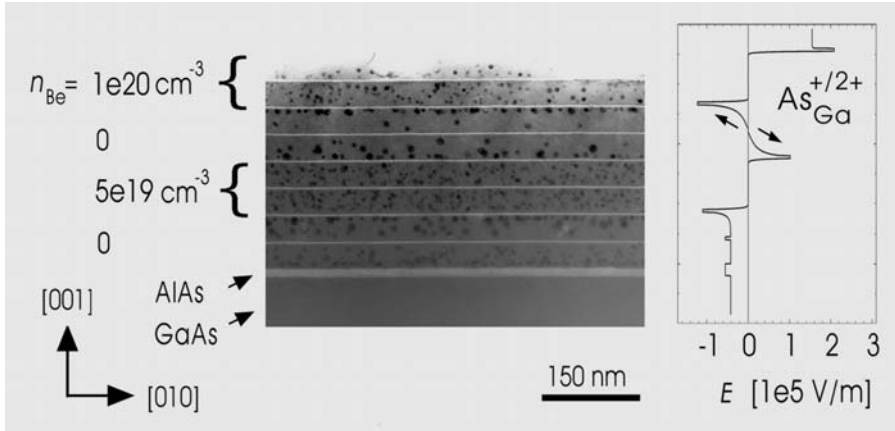


Fig. 3
Cross-sectional micrograph of a MQW sample annealed at 750°C for 30 min showing the formation of arsenic precipitates inside the LT-GaAs layers together with the associated electrical fields E assuming no compensation of acceptors.

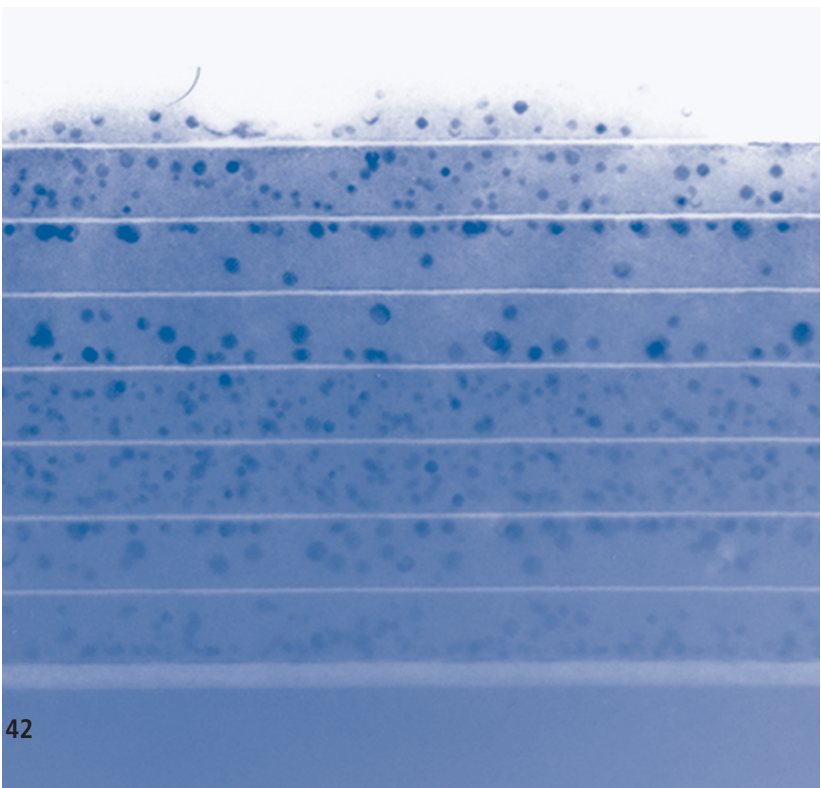
More detailed considerations on the electronic properties of the MQWs demonstrate that the observed increase of H quantities with increasing beryllium doping concentrations is well correlated with the dopant induced bending of the electronic bands, thus influencing the movement of charged gallium vacancies and, consequently, the intermixing. As illustrated in Fig. 3 by means of the electrical field distribution associated with an inhomogeneously MQW system, this “Fermi level effect” also plays a considerable role in the precipitation of excess arsenic. In this case, upon annealing the growth and ripening of the precipitates via material transport of positively charged arsenic antisite point defects As-Ga is significantly reduced in the beryllium doped areas of the LT-GaAs layers. Additionally, the formation of dopant-vacancy defect complexes whose binding energy would have to be captured to allow the diffusion of gallium vacancies may play a role in the stabilization of the MQWs against the intermixing of aluminium and gallium by thermal activation, while we find no evidence for variations in the pure nominal concentration of the gallium vacancies in individual layers as measured by positron annihilation experiments.

REFERENCES

- (1) "Direct compositional analysis of AlGaAs/GaAs heterostructures by the reciprocal space segmentation of high-resolution micrographs"
K. Tillmann, M. Luysberg, P. Specht and E.R. Weber
Ultramicroscopy **93** (2002), 123-137.
- (2) "High-resolution imaging with an aberration-corrected transmission electron microscope"
M. Lentzen, B. Jahnen, C.L. Jia, A. Thust, K. Tillmann and K. Urban
Ultramicroscopy **92** (2002), 233-242.
- (3) "Mechanisms of interdiffusion and thermal stability upon annealing of AlAs/GaAs:Be quantum wells grown under low temperature conditions"
K. Tillmann, M. Luysberg, P. Specht and E.R. Weber
Inst. Phys. Conf. Ser. No. **169** (2001), 101-108.

AUTHORS

Karsten Tillmann and Martina Luysberg



“Live” Observations of the Growth of Nanostructures

Electronic devices on the nanometer scale need new approaches and technologies for assembly and fabrication. One approach is the self assembly of nanostructures during strained layer growth with elastic stress as a driving force. In order to understand and to optimize the self assembly process, the complete growth procedure has to be studied in great detail.

All post growth characterization methods of thin films have disadvantages: The growth itself is not observed as a continuous process and the film morphology may change during cooling from growth temperature to room temperature. Therefore, the direct and local real time imaging of the film morphology during growth is highly desirable. We show that scanning tunneling microscopy can be used to observe nanostructures during growth.

Simultaneous scanning tunneling microscopy (STM) and epitaxial growth is used to access the evolution of semiconductor growth down to the atomic level. The complete characterization of the growth process allows the identification of fundamental growth processes and facilitates the comparison to theoretical models. For Si/Si(111) epitaxy the influence of surface reconstruction on growth leads to the formation of kinetically stabilized “magic” islands. The influence of strain on the growth morphology is shown for the case of heteroepitaxial growth of Ge on Si(001). The evolution of size and shape of three-dimensional islands reveals self limiting behavior which is explained by a kinetic growth model.

INTRODUCTION

Some of the growth-processes are displayed as movies. See:

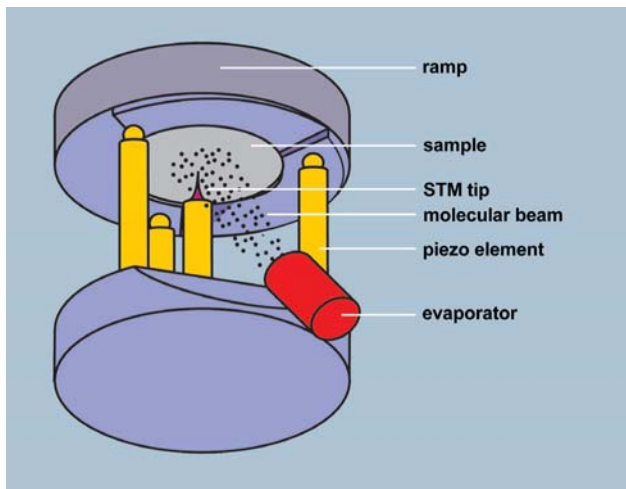
<http://www.fz-juelich.de/video/voigtlaender>



APPROACH

Today scanning tunneling microscopy routinely is used to image surfaces with a resolution down to the atomic level. Recently we expanded the capability of this method to observe the semiconductor growth processes live. The scanning microscopy of the surface with the STM tip is performed at high temperatures during the growth process (Fig. 1).

Fig. 1
Principle of the STM design which is used for simultaneous STM scanning and MBE growth at high temperatures.



An evaporator points to the heated sample which is located in the STM. Continuous imaging of the growing surface results in movies showing details of the growth process on the atomic level [1]. Some of the movies can be accessed in the internet: <http://www.fz-juelich.de/video/voigtlaender>.

RESULTS

"Magic" island sizes during Si growth

The influence of the surface reconstruction on epitaxial growth of Si on Si(111) could be determined. "Surface reconstruction" denotes the atomic arrangement at a surface. Typically it differs from the volume structure. Monoatomic high islands grow laterally in rows of the width of the 7x7 reconstruction unit cell. This can be seen in the growth sequence shown in Fig. 2. Scanning tunneling microscopic measurements performed during growth show the stability of complete rows [2]. It takes a long time before the nucleation of the next row starts. To nucleate the growth of a new row, a nucleation barrier has to be overcome.

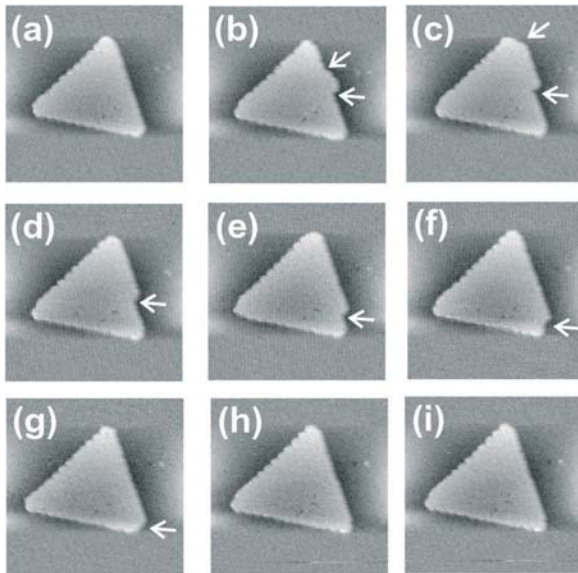


Fig. 2

Sequence of images showing the growth of a triangular Si island on Si(111). Rapid growth of the island in form of a row of the width of the (7x7) reconstruction is observed, as indicated by arrows ($T = 575\text{K}$, image size 500\AA).

<http://www.fz-juelich.de/video/voigtlaender>

During epitaxial growth the surface atoms become bulk atoms and the surface reconstruction has to be disassembled to rearrange the atoms into the bulk structure. For this process, an energy barrier has to be overcome. This nucleation barrier is different in different parts of the unit cell. A larger energy barrier is required to overgrow the faulted part (F) of the unit cell compared to the unfaulted part (U) of the reconstruction unit cell. A 2D island is only surrounded by faulted parts (F) of the unit cell (inset in Fig. 3). This leads to a barrier to nucleate a new row at

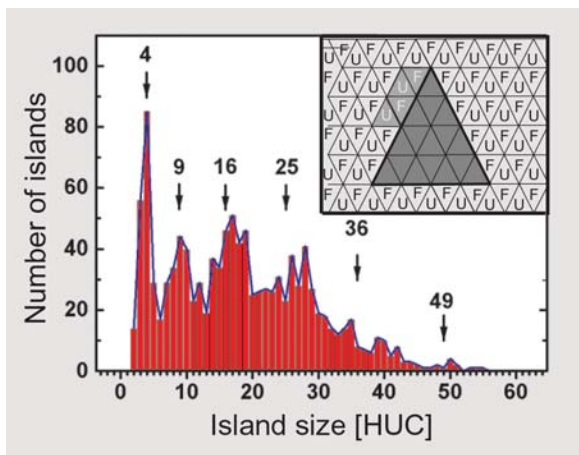


Fig. 3

Experimentally observed island size distribution with peaks at the "magic" sizes of 4, 9, 16, 25... half unit cells (HUC). These islands have closed shells corresponding to stable island sizes. The inset shows the schematic arrangement of the faulted (F) and unfaulted (U) unit cells around an island which is shown in the center.

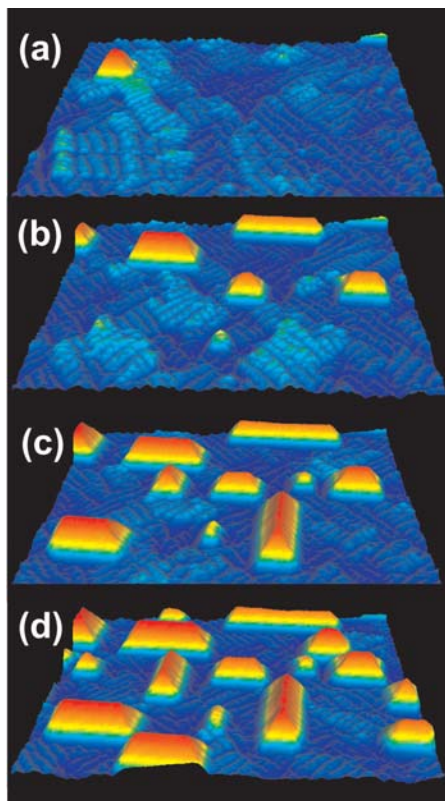


the island edge and explains the stability of a complete triangle as island form. The particular stability of islands with closed shells of the surface reconstruction leads to "magic" island sizes in the measured island size distribution. Peaks in the island size distribution are observed for the stable island sizes: 4, 9, 16, 25... half unit cells (HUC) (Fig. 3).

Hut cluster growth of Ge on Si

In heteroepitaxial growth of Ge on Si the strain in the Ge layer leads to the formation of three-dimensional islands after the formation of a thin Ge wetting layer. The evolution of nanometer sized strained Ge islands on Si(001) is studied during growth. Self limiting growth (slower growth for larger islands) of Ge hut clusters on Si(001) is observed. The growth behavior imaged by STM during epitaxial growth is shown as a growth sequence (Fig. 4).

Fig. 4
Images from a STM growth movie of Ge hut cluster growth. The same area is imaged repetitively with the STM during Ge growth at 575K. Details of the evolution of the growth morphology are observed. (Image size 2000 Å)



[http://www.fz-juelich.de/
video/voigtlaender](http://www.fz-juelich.de/video/voigtlaender)

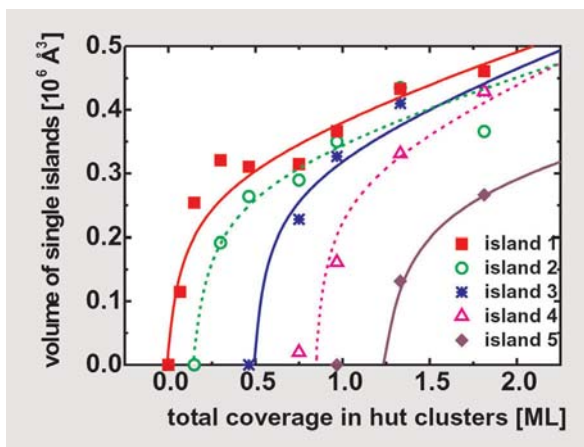


Fig. 5:
Evolution of the volume of
single hut clusters. The size
evolution shows self limiting
behavior for larger islands.



Imaging of the same area enables the observation of the same islands as function of coverage [4]. From such movies the evolution of the volume of hut clusters as function of time can be extracted (Fig. 5). The initial fast growth of the islands decreases with increasing size of the islands indicating self limited growth. The self limiting growth is induced by a nucleation barrier for the growth of a new layer on the facets of the hut shaped islands. The lines in Fig. 3 are calculated in a model featuring kinetically self limited growth, including a barrier for the nucleation of a new layer on a facet [4]. The kinetically limited slower growth for larger islands can lead to a desired narrow size distribution of Ge islands on Si.

We have demonstrated the ability to perform STM imaging during epitaxial growth at high temperatures. This allows the study of fundamental processes of Si and Ge epitaxy on Si surfaces. In particular, due to the high spatial resolution of the STM, it is possible to directly observe the influence of surface reconstruction on epitaxial growth which leads to the formation of kinetically stabilized "magic" islands in Si/Si(111) epitaxy. In hetero-epitaxial growth, the response of the film morphology to the misfit stress can be imaged directly. The growth of individual nanometer sized islands can be followed as function of coverage. A kinetically limited growth speed of larger islands is observed.

SUMMARY

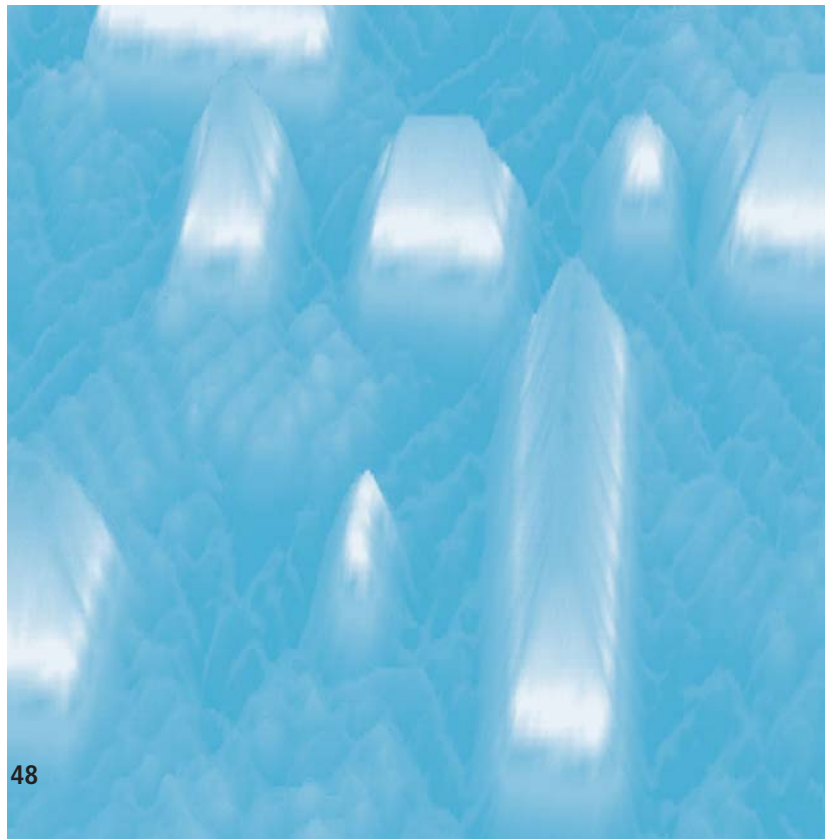


REFERENCES

- [1] "Fundamental processes in Si/Si and Ge/Si epitaxy studied by scanning tunneling microscopy during growth"
B. Voigtländer, Surface Sci. Rep. **43** (2001) 127
- [2] "Direct Observation of Sub-Critical Fluctuations during the Formation of Strained Semiconductor Islands"
D.E. Jesson, B. Voigtländer and M. Kästner,
Physical Review Letters **84** (2000) 330.
- [3] "Magic islands in Si/Si(111) homoepitaxy"
B. Voigtländer, M. Kästner, and P. Smilauer,
Phys. Rev. Lett. **81**(1998) 858
- [4] "Kinetically self-limiting growth of Ge islands on Si(001)"
M. Kästner and B. Voigtländer,
Phys. Rev. Lett. **82** (1999) 2745

AUTHOR

Bert Voigtländer



Nanowires and Nanorings at the Atomic Level

Nanometer sized electronic structures are highly desirable for the future miniaturization of electronic devices¹⁻³. To fabricate semiconductor devices of dimensions beyond the limits of lithography alternative methods have to be explored.

Self-organized growth of semiconductor nanostructures is one of these alternative approaches to build nanostructures bottom-up atom by atom with the help of nature. Recently, nanowires have attracted a lot of interest because they are required to interconnect functional units in nano- and molecular electronics. Smaller nanowires than the ones fabricated so far are desirable. Here we show that it is possible to grow Si and Ge nanowires with a width of 3.5 nm and a thickness of only one atomic layer (0.3 nm) by self-assembly. The cross section of these nanowires contains only about 21 Ge atoms. Generally the use of self-organization for the formation of nanostructures is limited to simple structures. Here we demonstrate, that more complex Si/Ge nanostructures, namely Si/Ge rings, can be grown by self-assembly, using a two-dimensional island growth geometry.

For the synthesis of Ge nanowires we use pre-existing step edges on the Si(111) surface as templates. If the diffusion of the deposited atoms is sufficient to reach the step edges, the deposited atoms attach themselves exclusively at the step edges and the growth proceeds by a homogenous advancement of the steps (step flow growth mode). If only small amounts of Ge are deposited, the steps advance just some nanometers and narrow Ge wires can be grown.

A key issue for the controlled fabrication of nanostructures consisting of different materials is a method of characterisation which can distinguish between the different materials on the nanoscale. In case of the important system Si/Ge it has been difficult to differentiate between Si and Ge due to their similar electronic structure. Here we use a new approach: The surface is

INTRODUCTION

Video on the web:
www.fz-juelich.de/video/voigtlaender

APPROACH



terminated with a monolayer of Bi, which allows to distinguish between Si and Ge. Both elements can be easily distinguished by the apparent heights in the scanning tunneling microscopy images. It turned out, that the apparent height measured by the STM is higher on areas consisting of Ge than on areas consisting of Si.

RESULTS

Figure 1a shows an STM image after a repeated alternating deposition of 0.15 atomic layers of Ge and Si, respectively, at a Si step edge. Due to the step flow growth Ge and Si wires are formed at the advancing step edge. The yellow stripes consist of Ge and the red stripes are areas consisting of Si. The assignment of Ge and Si wires is evident from the order of the deposited materials (Ge, Si Ge, Si and Ge, respectively in this case). The initial step position is indicated by white arrows in the right part of

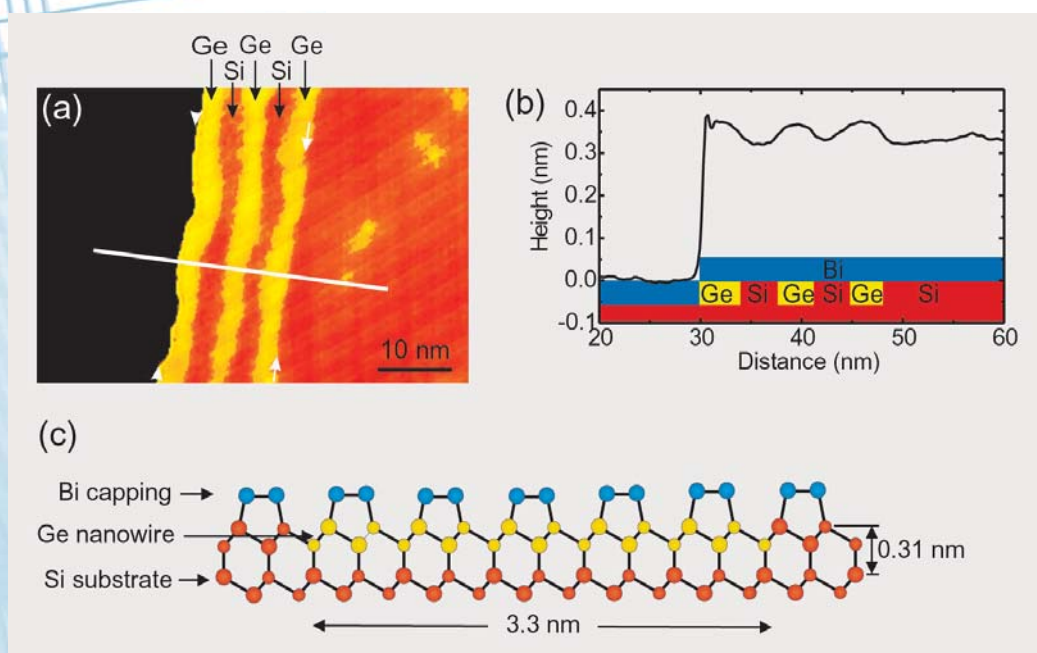


Fig. 1

(a) STM image of two-dimensional Ge/Si nanowires grown by step flow at a pre-existing step edge on a Si(111) substrate. Si wires (red) and Ge wires (yellow) can be distinguished by different apparent heights. (b) The cross section along the white line in (a) shows the dimensions of the Si and Ge nanowires. The width of the wires is ~ 3.5 nm and the height is only one atomic layer (0.3 nm). (c) Atomic structure of a 3.3 nm wide Ge wire (yellow atoms) on the Si substrate (red atoms) capped by Bi (blue). The cross section of the Ge wire contains only 21 Ge atoms.

Fig.1a. The step edge has advanced towards the left (arrow-heads in Fig.1a) after the growth of the nanowires. The apparent height of Ge areas is ~ 0.07 nm higher than the apparent height of Si wires (Fig.1b). The width of the Si and Ge wires is ~ 3.5 nm as measured from the cross section (Fig.1b). The nanowires are two-dimensional with a height of only one atomic layer (~ 0.3 nm). Therefore, the cross section of a 3.3 nm wide Ge nanowire contains only 21 atoms (Fig.1c).

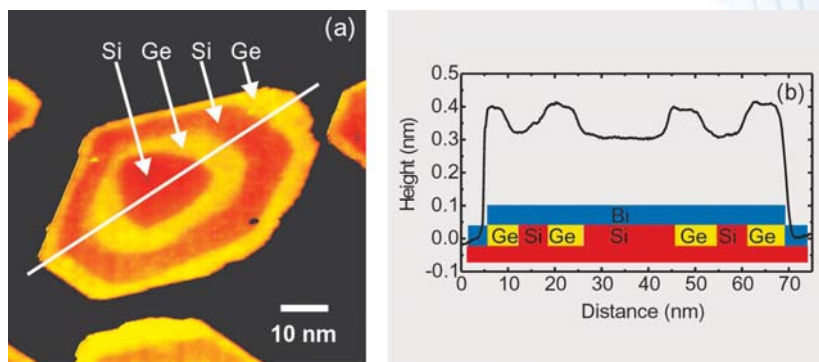


Fig. 2

(a) Two-dimensional Ge/Si ring structure imaged with the STM. Ge rings are shown as yellow and Si rings shown as red. The width of the rings is 5-10 nm and the height is one atomic layer (0.3 nm).

(b) Cross section along the line indicated in (a). Due to the Bi termination the Ge rings are imaged ~ 0.09 nm higher than the Si rings.

Using two-dimensional island growth, different types of Si/Ge nanostructures, namely Si/Ge ring structures can be grown by self-assembly (Fig.2a). In the two-dimensional island growth mode the diffusion of deposited atoms at the surface is reduced so that most of the diffusing atoms do not reach the step edges but nucleate as two-dimensional islands or attach to existing islands. Once islands of one atomic layer height have nucleated, deposited atoms diffuse towards the island edge and are incorporated forming a ring of Ge or Si, respectively (Fig.2a). A cross section indicating the measured height of the Si and Ge rings is shown in Fig.2b. The width of the rings is 5-10 nm and the thickness is only one atomic layer (0.3 nm).



SUMMARY

We have shown, that the controlled formation of different kinds of two-dimensional Si/Ge nanostructures, like nanowires, nanowire superlattices and nanorings is feasible. The nanostructures grown have a width down to 3.5 nm and a sub-nanometer thickness (0.3 nm), corresponding to a cross section consisting of only ~ 21 atoms. In spite of the sub-nanometer thickness the atoms building the Ge nanostructures are connected by strong lateral covalent bonds. The strong lateral bonds open exiting opportunities to observe charge transport through these nanostructures. A combination of nanorings and nanowires could be used to build more complex nanostructures and study charge transport in these structures. The controlled formation of such small nanostructures would be impossible without a material specific characterisation method on the nanoscale. A simple and general method has been presented to distinguish between Si and Ge in two-dimensional nanostructures using the height difference in STM images after termination of the surface with Bi.

REFERENCES

- [1] T. Ito and S. Okazaki, Pushing the limits of lithography Nature **406**, (2000) 1027.
- [2] E.S. Kim, N. Usami, and Y. Shiraki, Control of Ge dots in dimension and position by selective epitaxial growth and their optical properties, Appl. Phys. Lett. **72** (1998) 1617.
- [3] P. Kluth, Q.T. Zhao, S. Winnerl, S. Lenk, and S. Mantl, Fabrication of epitaxial CoSi_2 nanowires, Appl. Phys. Lett. **79** (2001) 824.

AUTHORS

Bert Voigtländer and Midori Kawamura

2D Supramolecular Electrochemistry and Nanostructures

The direct observation, manipulation and characterisation of molecules and their self-organised structures is a multidisciplinary challenge to develop new materials with unique and addressable properties. One of the main objectives comprises the formation and manipulation of structural and functional units in nanoscale dimensions. Impressive first examples are molecular switches and nanowires. This fascinating research is substantially influenced by new strategies of self-assembly and the fast development of high-resolution analytical tools, such as scanning probe microscopies. Supramolecular chemistry or the chemistry of the non-covalent intermolecular bonds, which involves recognition, transformation and translocation of information, is one of the main approaches to design functional molecular architectures. Possible structural motifs ("molecular information sources") are hydrogen-bonding, π -stacking and ion-ligand co-ordination. The creation of supramolecular nanostructures on surfaces bears unique potential to explore new surface phenomena and to tailor localised functions such as electron transport, molecular recognition or pathways of interfacial reactions.

Our strategy is based on the formation of monolayers of „informed“ molecules on electrified solid/liquid interfaces employing the concepts of supramolecular chemistry in two dimensions. The chosen electrochemical environment comprises that the electrode surface has to be considered (1) as a possible electron donor or acceptor as well as (2) an additional co-ordination centre. Combining electrochemical experiments with structure sensitive in situ techniques, such as scanning probe microscopy (STM) and spectroscopy (STS), surface X-ray scattering and vibrational spectroscopy we aim to develop an under-

INTRODUCTION

APPROACH





standing how an interfacial systems evolves from the macroscopic through the microscopic to an atomic or molecular level. Our first goal comprises the direct monitoring of the 2D assembly of the instructed molecules and ions on potentiostatically controlled surfaces with atomic/molecular resolution employing in-situ STM and STS. The second goal is focussed on the local addressing and tailoring of molecular and interfacial properties and functions, such as conductivity, electron transfer involving individual redox-centres or the recognition of molecular units.

RESULTS

Example 1 2D Self-organisation by directional hydrogen bonding and π -stacking

The first example deals with instructed hydrogen bonding. Uracil, a pyrimidine base, was potentiostatically deposited onto an uncharged Au(111) electrode from aqueous electrolyte. The analysis of the high-resolution STM-contrast pattern reveals a 2D network of planar oriented uracil molecules, interconnected by directional hydrogen bonds (Fig.1A). The self-assembly is critically dependent on the molecular structure. Substituting uracil with a methylgroup in 5 – position gives rise to the formation of one-dimensional zigzag patterns of hydrogen bonded ribbons (Fig.1B). The application of a positive electrical field triggers an orientational change of the organic molecule from planar to perpendicular to the surface. This field-induced structural transition is reversible. The final chemisorbed structures are determined by the co-ordination of one nitrogen atom of uracil with the underlying gold substrate and competitive π -stacking. This delicate interplay gives rise to a hexagonal, densely packed arrangement of interdigitated uracil rows on the hexagonal Au(111) – electrode (Fig.1C). A completely different stick-like pattern was found on the quadratic Au(100) surface (Fig.1D).

The demonstrated ability of uracil and its derivatives to form ordered 2D supramolecular structures of „instructed“ molecules on Au(hkl) via N – co-ordination and π -stacking is a general property of aromatic heterocyclic molecules on metal electrodes. Exploiting these structural motifs further guides to the systematic construction of tailored organic host lattices on surfaces.

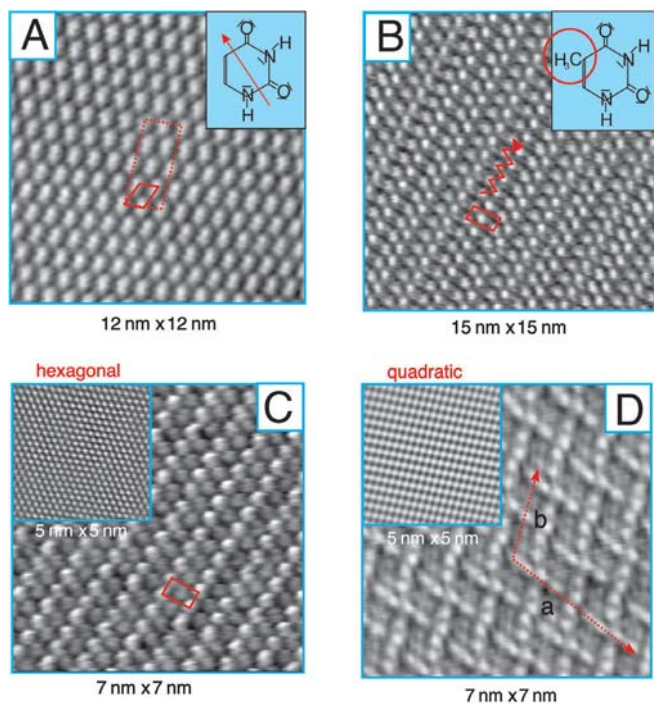


Fig. 1
STM-images of selfassembled hydrogen-bonded adlayers of uracil (A) and 5-methyluracil (B) on Au(111)/0.1 M H₂SO₄ at 0.0 V. (C) and (D) show the field-induced chemisorbed stacking phases of uracil on Au(111) (C) and Au(100) (D) at 0.5 V. The unit cells are indicated [1].

Fabrication of surface supported nanostructures with 2,2'-bipyridine on Au(hkl)

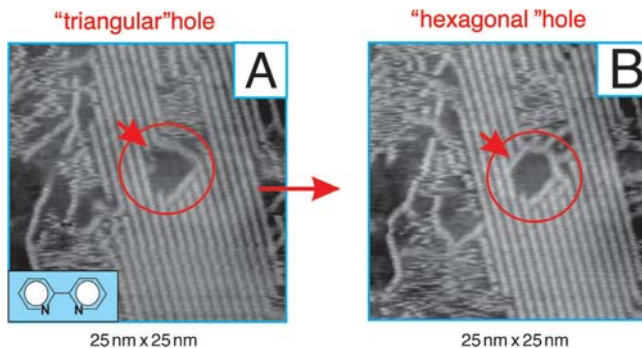
Example 2

The organic molecule 2,2'-bipyridine forms selforganized „molecular chains“ on Au(111) electrodes (Fig.2A). Defect free areas of the surface are covered by long range ordered parallel molecular rows. The presence of monatomically deep holes, such as generated by selective substrate oxidation/reduction cycles, causes the creation of a network of correlated, but loosely packed molecular chains. Single chains decorate the periphery of holes, and trigger the local field-induced switching of the shape. The molecule-induced morphological change of a trigonal into a hexagonal shaped hole is depicted in Fig.2.

Employing the reconstruction elements we could selectively decorate an Au(100) electrode with 2,2'-bipyridine. The experiment started with an ideally terminated Au(100)-(1 x 1) surface. Applying a negative potential partially reconstructs the surface. A snapshot is presented in Fig. 3A. The electrode exhibits sepa-

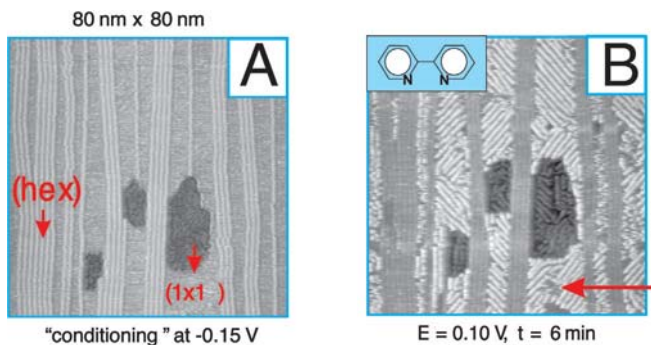


Fig. 2
Adsorbate-induced shape change of a monatomically deep substrate defect from triangular to hexagonal. System: 2,2'-bipyridine on Au(111) in 0.05 M H₂SO₄.



rated patches with hexagonal symmetry (hex) and such with quadratic (1 x 1) symmetry. Therefore, it is energetically and structurally inhomogeneous. Adding organic molecules, such as 2,2'-bipyridine, which binds via N – co-ordination to the gold surface, demonstrates that only the (1 x 1) surface patches are covered (Fig. 3B). The long range order of the molecular stacks increases with observation time. The selective decoration of the (1 x 1) regions reflects the local positive surface excess charge of (1 x 1) with respect to (hex).

Fig. 3
Nano-decoration of a structured Au(100) with 2,2'-bipyridine in 0.05 M H₂SO₄ employing partial substrate reconstruction [2].



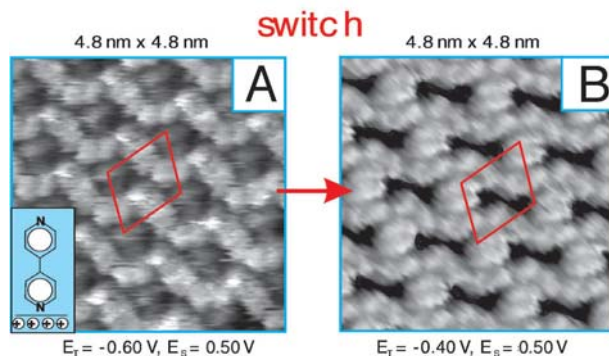


Fig. 4:
Contrast inversion of the
high-coverage 4,4'-bipyridine
stacking structure on
Au(111) in 0.05 M KClO₄ as
a function of the applied
tunnelling conditions [3].

Potential-induced molecular switching

4,4'-bipyridine acts as a bridging "electron shuttle" in electron transfer reaction. The interfacial orientation of 4,4'-bipyridine on Au(111) electrodes can be reversibly tuned with the applied electrode potential from all-perpendicular towards inclined and planar. Fig.4 illustrates, as an example, typical high resolution STM-experiments of the high coverage phase. The complex fine structure scales with the geometries of the molecule and of the substrate surface, respectively. Upon changing the potential applied to the STM-tip we observed dramatic changes of the STM-contrast pattern at fixed substrate potential (Fig. 4A and 4B). The latter indicates that the electron transfer between tip and sample is mediated by the π -system of the molecules, e.g. through-bond tunnelling occurs. 4,4'-bipyridine acts as a potential-driven molecular switch.

Example 3

In-situ Scanning tunnelling spectroscopy and perspectives

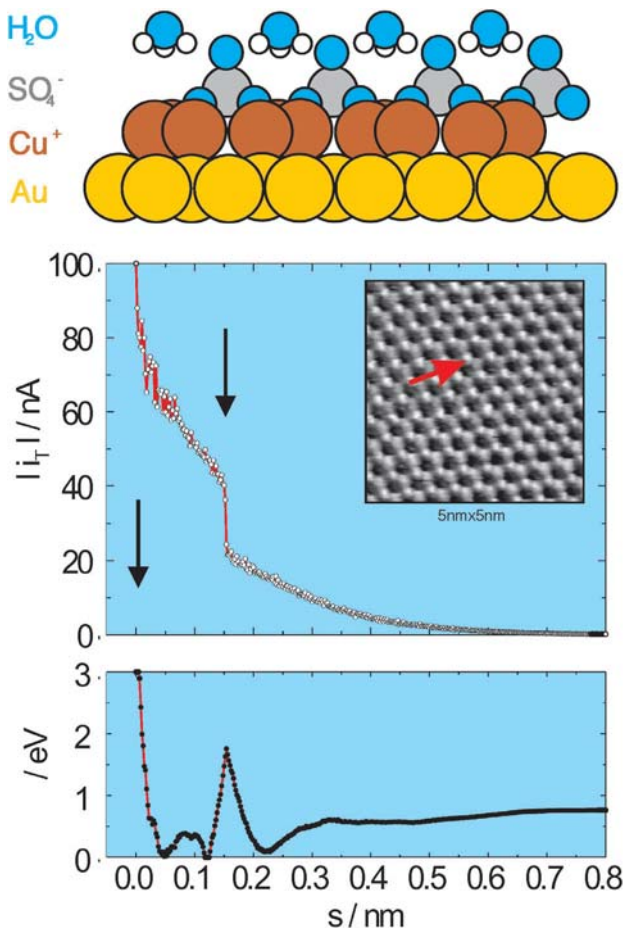
Although in-situ STM measurements reveal electronic structure information, separating the contributions of electronic and geometrical properties is not straightforward. Electronic structure information is more directly accessible from scanning tunnelling spectroscopy (STS), such as measurements of current voltage ($i_T - V_T$) and current-distance ($i_T - \Delta s$) characteristics. Therefore,

Example 4



we implemented in situ STS at electrochemical solid/liquid interfaces. For the first time, we succeeded to combine high resolution STM with simultaneous STS ($i_T - \Delta s$) measurements at a fixed adlayer location. As an example, Fig. 5 illustrates a typical $i_T - \Delta s$ trace, as measured on top of a coadsorbed sulphate, and the barrier height profile obtained for a $(\sqrt{3} \times \sqrt{3})R30^\circ$ copper layer co-assembled with sulphate ions onto an Au(111) electrode [4].

Fig.5:
STS spectroscopy in solution ($i_T - \Delta s$ characteristics) and calculated one-dimensional potential barrier height profile ($\phi - \Delta s$) as obtained for the ordered Cu – UPD ($\sqrt{3} \times \sqrt{3}$) R 30° phase on Au(111) at $E = 0.15$ V vs. Cu/Cu $^{2+}$. The position of the $i_T - \Delta s$ measurement is indicated by the red arrow in the STM-image. The corresponding topographic image and a model of the adlayer structure are shown as insets. The copper ions are coadsorbed with sulphate and water species [4].



REFERENCES

- [1] Th.Dretschkow, Th.Wandlowski,
Topics Appl. Phys. 85 (2003) 259
- [2] Th.Dretschkow, Th.Wandlowski,
J. Electroanal. Chem. 467 (1999) 207
- [3] D.Mayer, Th.Dretschkow, K.Ataka, Th.Wandlowski;
J. Electroanal.Chem., 524-525 (2002) 20
- [4] G.Nagy, Th. Wandlowski,
Phys. Chem. Commun. 5 (2002) 112;
Z. Phys. Chem., 217 (2003) 587

**Thomas Dretschkow, Dirk Mayer, Gabor Nagy,
Thomas Wandlowski**

AUTHORS

Fullerenes: Tailored Molecules for New Materials

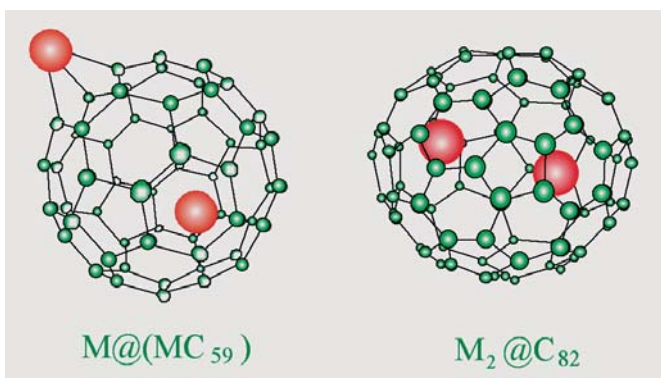
INTRODUCTION

Fullerenes are caged carbon clusters of high chemical stability, in which carbon atoms are situated at the vertices of exactly 12 pentagons and – depending on the cluster size – a differing number of hexagons. The total number of cage atoms is even, each being threefold coordinate. The most prominent example of a fullerene is the soccer ball shaped C_{60} cluster which comprises 20 hexagons. Its discovery was in 1996 awarded with the Nobel Prize for Chemistry to Kroto, Curl and Smalley.

Fullerenes offer possibilities to engineer exceptional new materials. By alkali doping solid C_{60} can become metallic and even superconducting with transition temperatures as high as 33 K. In these materials the C_{60} clusters occupy positions of an fcc-lattice and the alkali dopants occupy interstitial lattice sites. Moreover, other types of doping are possible where the dopant is either incorporated in the network of the fullerene cage or

Fig.1

Fullerene cages can be doped in several ways. Dopant atoms can replace a carbon atom in the cage network or can be endohedrally captured. Such entities are denoted $M@C_n$ where M is the metal atom and C_n the carbon cage. Larger carbon cages may even encapsulate several atoms as exemplarily shown for $M_2@C_{82}$. In the superconducting alkali fullerenes the alkali atoms occupy interstitial lattice sites in a C_{60} single crystal (exohedral doping).



even endohedrally captured inside (Fig.1). Larger fullerene cages can even incorporate several atoms or small molecules. Endohedral fullerenes are therefore symbolized by the chemical formula $M_m@C_n$, where M_m is the encapsulated particle and C_n denotes the carbon cage.

Endohedral metallofullerenes have been found to be very stable even in air and even when doped with the otherwise very reactive rare-earth atoms. Due to the charge transfer from an encapsulated metal atom to the π -electron system of the carbon cage such materials may form metallic or even superconducting or ferromagnetic materials. Theory predicts that the encapsulated metal atoms occupy acentric equilibrium positions with respect to the carbon cage. When strongly hybridized with the carbon cage this may lead to permanent dipole moments and suggests that ferroelectric properties may also become possible.

Fullerenes are produced from graphite or graphite composite rods by laser ablation or electric arc discharge followed by condensation in an inert gas atmosphere. At present, most of them can be formed in microscopic amounts only. Therefore such compounds are often studied in the gas phase in mass selected cluster beams or after mass selection deposited in small amounts on a solid surface.

On the surface the electronic structure of individual particles can be studied by scanning tunneling spectroscopy. A chemically etched tungsten tip is kept at a fixed small distance from the individual cluster. To take a spectrum, an applied voltage between the tip and the substrate is continuously tuned and the tunneling current measured. This technique can locally monitor both the occupied and unoccupied density of states in the vicinity of the Fermi level E_F ($\sim E_F - 2\text{eV}$ to $\sim E_F + 2\text{eV}$). The total electron-binding-energy spectral range can be probed when the coverage exceeds about one tenth of a monolayer. Then photoemission spectroscopy and photoabsorption spectroscopy with synchrotron radiation become applicable. Due to its tunability synchrotron radiation has the additional advantage to resonantly enhance the sensibility for any localized electronic density of states of the metal atom. In the following we will discuss three examples of fullerenes which in the given order are available in increasing amounts.

APPROACH



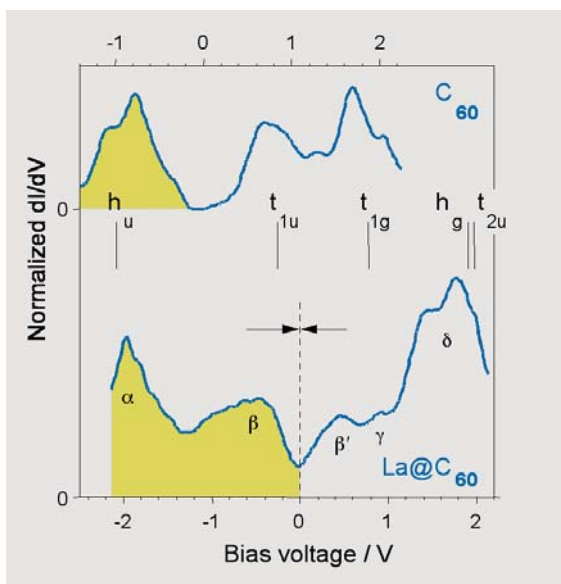
RESULTS

La@C₆₀

La@C₆₀ deposited as isolated clusters onto a graphite substrate shows metallic behaviour as observed by I(V) curves taken locally with an STM tip placed directly above the cluster. Fig. 2 compares the normalised differentiated I(V) curves, the so called tunneling spectra of C₆₀ and La@C₆₀, which theoretically are proportional to the local densities of states. The molecular orbitals as calculated for pristine C₆₀ and given in the middle of the figure can still be identified in both spectra. The Fermi level (0V) for La@C₆₀ is shifted to the t_{1u} orbital due to the charge transfer.

Fig.2

Normalised differential tunneling conductivities (dI/dV)(V/I) at room temperature of C₆₀ (top) and La@C₆₀ (bottom) on HOPG (highly oriented pyrolytic graphite) as a function of the bias voltages. The C₆₀ derived molecular orbitals can still be assigned (middle). The Fermi level (0V) of La@C₆₀ (lower scale) is shifted with respect to that of C₆₀ (upper scale) due to the charge transfer from the lanthanum atom to the Carbon cage. While C₆₀ shows a gap at the Fermi level La@C₆₀ does not. This is even more clearly demonstrated in Fig. 3.



While C₆₀ shows a gap at the Fermi level La@C₆₀ does not. Thus La@C₆₀ shows metallic behaviour. This is even more clearly visible in the I(V) curves of Fig. 3 which between room temperature and 29 K show a positive conductivity at 0 V. At 28 K a small gap of 40 mV opens which is attributed to a freezing of the dynamics of the lanthanum atom inside the carbon cage. The metal – like density of states in La@C₆₀ can be interpreted in terms of charge donation from the La atom into C₆₀ – derived π orbitals. Nominally La is expected to transfer three valence electrons into the threefold degenerate t_{1u} orbital of the fullerene cage. Therefore, one would expect solid La@C₆₀ to be

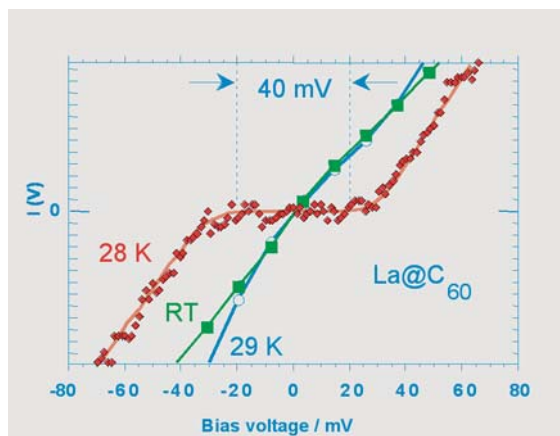


Fig. 3

Tunneling current of La@C_{60} on HOPG as a function of the bias voltage for three different temperatures. The positive conductivity at the Fermi level (0V) identifies the metallic character in the range between room temperature (RT) and 29K. A small gap of 40 mV opens at a transition temperature of $\sim 28\text{K}$. This was attributed to a freezing of the dynamics of the lanthanum atom inside the fullerene cage (1).

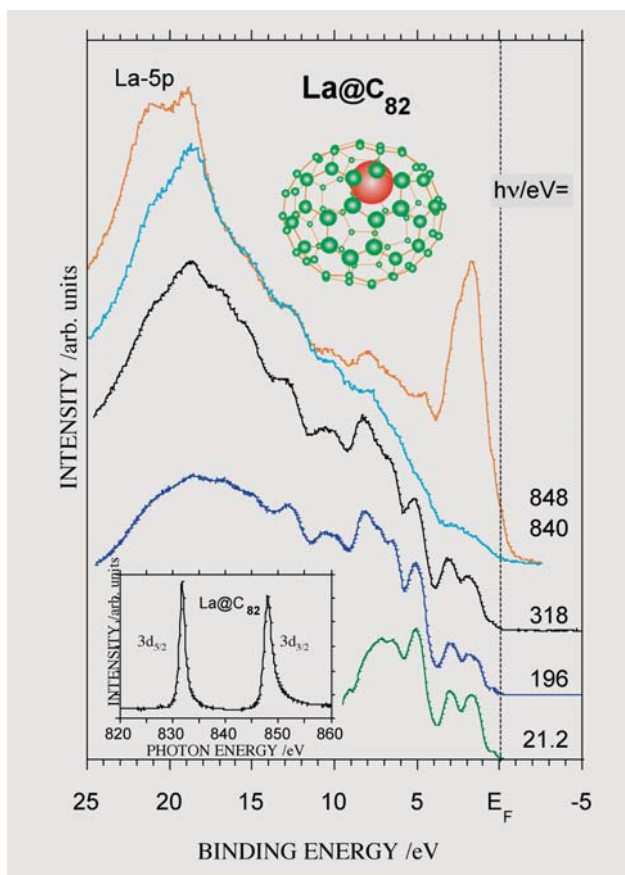
metallic. However, this simple approach is too easy because electron correlation effects are completely neglected in this simple picture. In fact, the electron-electron repulsion is so strong in doped fullerenes that a transition to a Mott-Hubbard insulator is observed in many other doped fullerenes. In this respect La@C_{60} rather is an exception than the norm. It is in fact the first endohedral fullerene with metallic character.

La@C_{82}

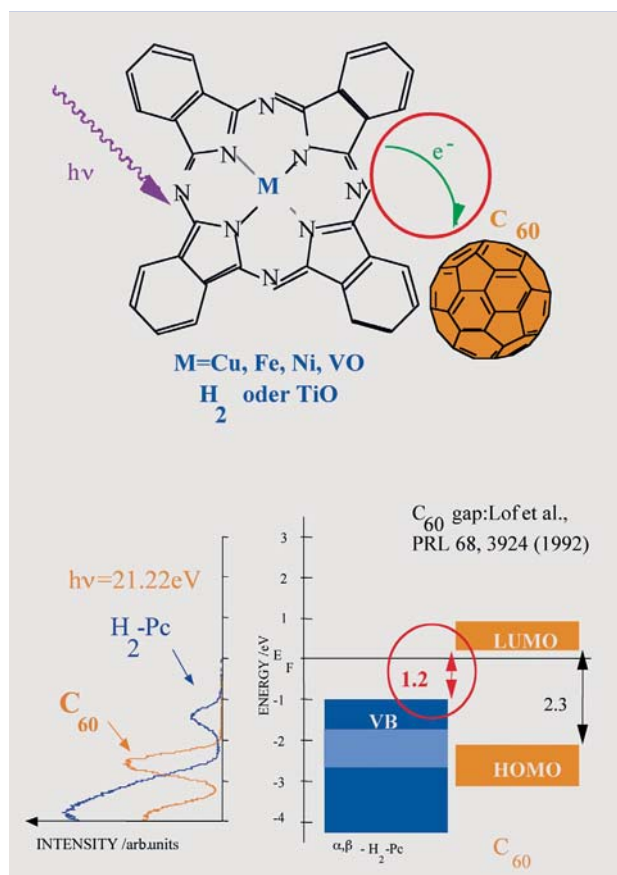
La@C_{82} belongs to the few endohedral fullerenes that have already been produced in mg quantities by extraction from fullerene soot and chromatographic separation. Therefore thin film samples of this semiconducting material can readily be prepared for photoemission spectroscopy. The interesting question here is whether the La atoms are in a 3+ state, transferring all valence electrons to the carbon cage. It is, however, difficult to spectroscopically identify the valence orbitals of only one La atom among those of 82 carbon atoms. However, by the use of tunable synchrotron radiation one can take advantage of the fact that, when exciting with photon energies in the La $3d_{5/2}$ and $3d_{3/2}$ core level resonances (see inset of Fig.4), the photoemission signal of the La-specific valence orbitals can be increased by a factor of up to 50. The photon energy is chosen such that a La 3d core electron is excited to an unoccupied La-4f level. Then the usual valence band photoemission spectrum is superposed by an Auger-like decay of this 4f state (here: reoccupation of the

Fig. 4

Valence-band photoemission spectra of $\text{La}@\text{C}_{82}$ at various photon energies (2). The spectra were taken with tunable synchrotron radiation, the spectrum at the bottom with a He-lamp. The topmost spectrum at 848 eV demonstrates the resonant enhancement of La-derived states. The apparent nonzero intensity at the Fermi level is due to a reduced energy resolution at this photon energy and not to a metallic character of the sample. This spectrum and the spectrum at 840 eV (blue line) are normalized in the binding-energy region between 12 and 18 eV. The inset shows the X-ray absorption (XANES) in the vicinity of the $\text{La-3d}_{3/2}$ $3d_{5/2}$ core excitation thresholds. From the resonant intensities it is estimated that about one third of an electron charge is left in the La-valence orbitals for $\text{La}@\text{C}_{82}$ and that the La-valence electrons are not completely delocalized on the fullerene cage.



core hole and simultaneous emission of a valence electron resulting in a remaining hole in the valence band). As both processes are leading to the same final state this results in an interference of two coherent decay channels. The cross section, however, is dominated by the Auger-like process. This way it is possible to demonstrate that the charge transfer is not complete in $\text{La}@\text{C}_{82}$ and that there is a sizeable hybridization of the electronic states of the La atom and the p-valence orbitals of the fullerene cage (Fig. 4). The La valence electrons are not completely delocalized on the fullerene cage. About 1/3 of an electron charge is left in the La-valence orbitals.



Enhanced photoconductivity in C_{60} doped phthalocyanines

C_{60} is the most abundant fullerene and can be produced in kg quantities. It is a strong electron acceptor since it is able to gather six electrons in its threefold degenerate t_{1u} LUMO (lowest unoccupied molecular orbital). This property can be used to improve the efficiencies of organic photo-conducting materials like e.g. the phthalocyanines. These materials are essential constituents of the photosensitive layers of photocopy machines and laser printers. In these layers a photon generates a pair of charges, an electron and a hole, and an exciton is formed. For the printing process these charges need to be separated and their recombination needs to be suppressed. The hole needs to diffuse to the surface of the layer to discharge it so that the

Fig. 5

Top: Scheme illustrating the charge transfer from a photo-excited phthalocyanine molecule to C_{60} . Bottom: Comparison of the energetic positions of UPS-features of C_{60} and $\tau\text{-H}_2\text{Pc}$ with the corresponding energy schemes (of H_2Pc and C_{60}) in the vicinity of the optical gap (3). The charge separation of the singlet excitonic state can be strongly improved when the sample is doped with C_{60} . Doping enhances the photoconductivity by a factor of 20. The position of the LUMO (lowest unoccupied molecular orbital) of C_{60} is below the excitonic excitation energy of H_2Pc . Therefore a separation of the electron and the hole and a transfer of the electron to C_{60} becomes favorable. This results in a more effective charge separation and thus a larger photocurrent of the C_{60} -doped sample.

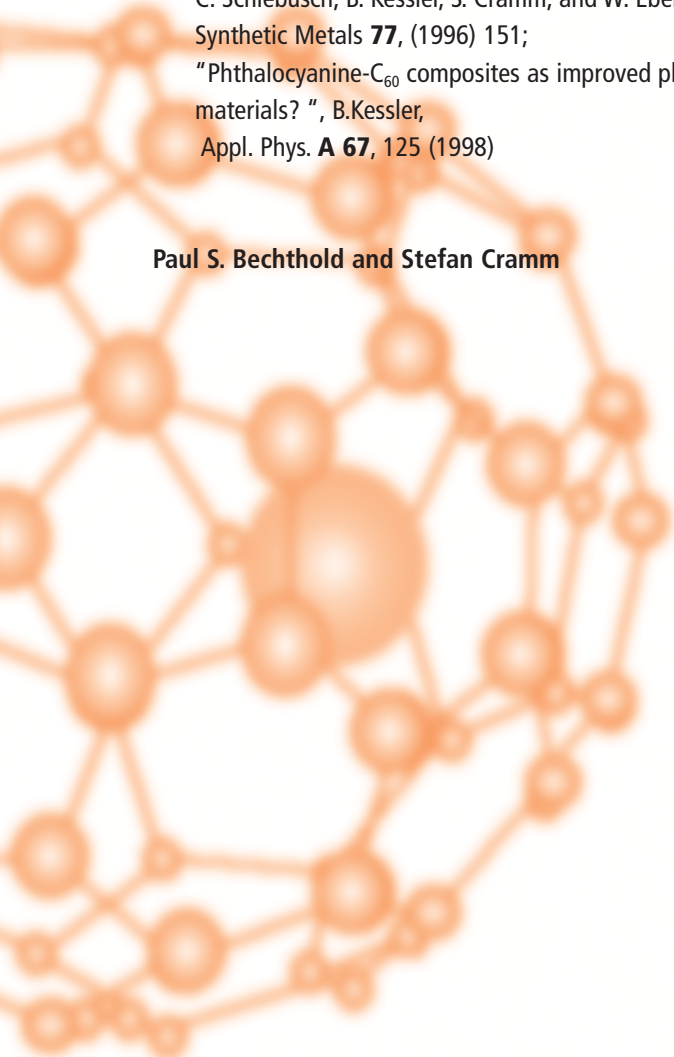


toner can not stick to it in that position. The electron diffuses to the metal backing. Due to its strong electron affinity C_{60} helps to enhance the charge separation. A necessary condition for a successful charge transfer is that the charge-separated state is energetically favored with respect to the excitonic state.

Thus the dopant molecules need to offer unoccupied states at energies below the exciton excitation energy. Another condition is that the dopant does not strongly interact with the photoconductor because this could inhibit the whole process. To verify these conditions the electronic structure of the phthalocyanine (here $\tau\text{-H}_2\text{Pc}$) in contact with C_{60} needs to be studied.

Information about the occupied states is obtained by photoelectron spectroscopy with ultraviolet radiation (UPS). The position of the unoccupied states can be deduced from the X-ray absorption fine structure (XANES). Both Methods are sensitive to possible chemical reactions of the constituents. In the case of non-reactivity the spectra of the composite are simply superpositions of the spectra of the constituents. Both above conditions have been verified for C_{60} doped phthalocyanines. The exciton recombination rates can be strongly reduced. The doping results in an increase of the photoconductivity of the photosensitive layer by more than one order of magnitude. This effect was explained by a very fast charge separation due to the high electron affinity of C_{60} .

As soon as more effective methods for large-scale production of fullerenes become available, the design of novel fullerene-based materials such as molecular metals of extremely low weight with magnetic or superconducting properties or as novel catalytic materials will be possible.

- 
- (1) "La@C₆₀: A metallic endohedral fullerene",
R. Klingeler, G. Kann, I. Wirth, S. Eisebitt, P.S. Bechthold,
M. Neeb, and W. Eberhardt,
J. Chem. Phys. **115**, (2001) 7215
- (2) "Evidence for incomplete charge transfer and La-derived
states in the valence bands of endohedrally doped La@C₈₂",
B. Kessler, A. Bringer, S. Cramm, C. Schlebusch, W. Eberhardt,
S. Suzuki, Y. Achiba, F. Esch, M. Barnaba, and D. Cocco,
Phys. Rev. Lett. **79**, (1997) 2289
- (3) "Organic photoconductors and C₆₀",
C. Schlebusch, B. Kessler, S. Cramm, and W. Eberhardt,
Synthetic Metals **77**, (1996) 151;
"Phthalocyanine-C₆₀ composites as improved photoreceptor
materials? ", B. Kessler,
Appl. Phys. **A 67**, 125 (1998)

Paul S. Bechthold and Stefan Cramm

REFERENCES

AUTHORS



